BRNO UNIVERSITY OF TECHNOLOGY

VYSOKÉ UČENÍ TECHNICKÉ V BRNĚ

FACULTY OF MECHANICAL ENGINEERING

FAKULTA STROJNÍHO INŽENÝRSTVÍ

INSTITUTE OF PHYSICAL ENGINEERING

ÚSTAV FYZIKÁLNÍHO INŽENÝRSTVÍ

MATERIAL CHARACTERIZATION AND MODELING OF INTERBAND CASCADE LIGHT EMITTING DIODES

MATERIÁLOVÁ CHARAKTERIZACE A MODELOVÁNÍ MEZIPÁSOVÝCH KASKÁDOVÝCH SVĚTELNÝCH DIOD

MASTER'S THESIS

DIPLOMOVÁ PRÁCE

AUTHOR — Bc. Kristína Herzánová

AUTOR PRÁCE

SUPERVISOR — Dr.techn. Ing. Hermann Detz

VEDOUCÍ PRÁCE

BRNO 2024

BRNO UNIVERSITY OF TECHNOLOGY
FACULTY OF MECHANICAL ENGINEERING

Assignment Master's Thesis

Institut:	Institute of Physical Engineering
Student:	**Bc. Kristína Herzánová**
Degree programm:	Physical Engineering and Nanotechnology
Branch:	no specialisation
Supervisor:	**Dr.techn. Ing. Hermann Detz**
Academic year:	2023/24

As provided for by the Act No. 111/98 Coll. on higher education institutions and the BUT Study and Examination Regulations, the director of the Institute hereby assigns the following topic of Master's Thesis:

Material Characterization and Modeling of Interband Cascade Light Emitting Diodes

Brief Description:

Following the success of quantum cascade lasers and detectors, their interband cascade counterparts are currently an area of active research [1]. While these devices offer operation at shorter wavelengths and a higher efficiency in general, the material system, including growth processes, parameters, and corresponding models, is not yet fully mature. A careful optimization cycle from the epitaxial growth to material characterization and modeling is required to establish this novel class of devices. Interband Cascade Light Emitting Diodes provide a logical first goal to study novel materials and pave the way for laser and detector devices.
This thesis will be composed of two major parts, completed at CEITEC and TU Wien (Austria). First, semiconductor heterostructures based on novel III–V materials will be provided by TU Wien and characterized at the visible and mid–infrared ellipsometry setups in the CEITEC Nano Core Facilities. The material parameters that are determined experimentally within this step will be necessary to develop a realistic device model in the second part. This model is based on a software package that has been developed in–house at TU Wien for cascaded semiconductor heterostructures using a self–consistent semi–classical rate equation model as described in [2]. Extensions were recently implemented to describe peculiarities that arise in the valence band for an interband cascade laser transport model [3]. The tasks to be completed within this thesis are an adaptation for radiative recombination for the modelling tool. Further implement the changes to the tool and establish tests. In the course of first simulations, the student together with the research group will identify further required modifications and implement them after evaluation of their impact. Later on, the student should adjust parameters and look into new designs foroptoelectronic interband devices. Through this hands–on experience on designing optoelectronicdevices the student will gain further intuitive knowledge on limits and possibilities of suchstructures. The student should implement additional effects into the tool, that enable furtherapplications.

Master's Thesis goals:

1. Extract material parameters for interband–cascade structures from ellipsometry measurements
2. Extend the existing transport model for radiative recombination
3. Verify model and optimize device structures

Recommended bibliography:

MEYER, Jerry; BEWLEY, William; CANEDY, Chadwick; KIM, Chul; KIM, Mijin et al. The Interband Cascade Laser. Photonics. 2020, roč. 7, č. 3. ISSN 2304-6732. Dostupné z: https://doi.org/10.3390/photonics7030075.

JIRAUSCHEK, Christian a KUBIS, Tillmann. Modeling techniques for quantum cascade lasers. Applied Physics Reviews. 2014, roč. 1, č. 1. ISSN 1931-9401. Dostupné z: https://doi.org/10.1063/1.4863665.

KNÖTIG, Hedwig; NAUSCHÜTZ, Josephine; OPAČAK, Nikola; HÖFLING, Sven; KOETH, Johannes et al. Mitigating Valence Intersubband Absorption in Interband Cascade Lasers. Laser & Photonics Reviews. 2022, roč. 16, č. 9. ISSN 1863-8880. Dostupné z: https://doi.org/10.1002/lpor.202200156.

Deadline for submission Master's Thesis is given by the Schedule of the Academic year 2023/24

In Brno,

L. S.

prof. RNDr. Tomáš Šikola, CSc. Director of the Institute	doc. Ing. Jiří Hlinka, Ph.D. FME dean

Abstract

This thesis focuses on the material and loss characterization of heterostructures used in interband cascade devices and the modeling of interband cascade light-emitting devices (ICLEDs). Interband cascade devices, particularly lasers and light-emitting diodes, are critical for mid-infrared photonic applications due to their efficient operation and potential for integration into photonic circuits. The study involves extracting material parameters from spectroscopic ellipsometry and FTIR measurements, and extending an existing transport model to account for radiative recombination processes, specifically the spontaneous emission in ICLEDs. Among the different loss mechanisms in these devices, particular attention was given to the valence intersubband absorption, which degrades the operation of interband cascade devices in the mid-infrared wavelength region above 4 m. The results, obtained through experimental characterization of interband cascade laser (ICL) waveguides examining their transmission losses, demonstrated the impact of valence intersubband absorption under various operating conditions. This research contributes to the optimization of interband cascade structures, leading to enhanced performance and broader applicability in sensing, environmental monitoring, and biomedical diagnostics.

Abstrakt

Tato práce se zaměřuje na charakterizaci materiálů a ztrátových mechanismů heterostruktur používaných v mezipásových kaskádových zařízeních a na modelování mezipásových kaskádových elektroluminiscenčních diod (ICLED). Mezipásová kaskádová zařízení, zejména lasery a elektroluminiscenční diody, mají zásadní význam pro fotonické aplikace ve střední infračervené oblasti vzhledem k jejich efektivitě a možnosti integrace do fotonických obvodů. Studie zahrnuje extrakci materiálových parametrů ze spektroskopické elipsometrie a FTIR měření a rozšíření stávajícího transportního modelu o zářivé rekombinační procesy, konkrétně o spontánní emisi v ICLED. Z různých ztrátových mechanismů v těchto zařízeních byla zvláštní pozornost věnována valenční mezipásové absorpci, která zhoršuje výkon mezipámových kaskádových zařízení v oblasti středních infračervených vlnových délek nad 4 m. Výsledky získané na základě experimentální charakterizace vlnovodů tvořených mezipásovými kaskádovými lasery (ICL) zkoumající jejich přenosové ztráty prokázaly vliv valenční mezipásové absorpce za různých operativních podmínek. Tento výzkum přispívá k optimalizaci struktur mezipásových kaskádových struktur, která vede ke zvýšení výkonu a širší použitelnosti v oblasti detekce, monitorování životního prostředí a biomedicínské diagnostiky.

Keywords

Interband Cascade Light Emitting Device (ICLED), Interband Cascade Laser (ICL), heterostructures, mid-infrared, material characterization, ellipsometry, spectroscopic techniques, waveguide characterization, valence intersubband absorption, recombination, spontaneous emission

Klíčová slova

Mezipásové kaskádové elektroluminiscenční zařízení, mezipásový kaskádový laser, heterostruktury, střední infračervená oblast, materiálová charakterizace, elipsometrie, spektroskopické techniky, charakterizace vlnovodu, valenční mezipásová absorpce, rekombinace, spontánní emise

HERZÁNOVÁ, K.: *Material Characterization and Modeling of Interband Cascade Light Emitting Diodes.* Brno University of Technology, Faculty of Mechanical Engineering, 2024. 51 s. Supervisor: Dr.techn. Ing. Hermann Detz.

I declare that I have written the Master's Thesis titled "Material Characterization and Modeling of Interband Cascade Light Emitting Diodes" independently, under the guidance of the advisor and using exclusively the technical references and other sources of information cited in the thesis and listed in the comprehensive bibliography at the end of the thesis.

As the author I furthermore declare that, with respect to the creation of this Bachelor's Thesis, I have not infringed and copyright or violated anyone's personal and/or ownership rights. In this context, I am fully aware of the consequences of breaking Regulation § 11 of the Copyright Act No. 121/2000 Coll. of the Czech Republic, as amended, and of any breach of rights related to intellectual property or introduced within amendments to relevant Acts such as the Intellectual Property Act or the Criminal Code, Act No. 40/2009 Coll., Section 2, Head VI, Part 4.

Kristína Herzánová

Thank you.

Kristína Herzánová

Contents

1. Introduction

Semiconductor lasers represent an important milestone in laser technology. One of the first semiconductor lasers was realized using a GaAs p-n junction [1], utilizing the radiative recombination in the depletion region to provide optical gain. Soon, advancements led to exploration of other semiconductor materials similar to GaAs, such as InAs, InP, AlSb and their alloys, facilitating lasers at different emission wavelengths spanning from the visible to the infrared region of the electromagnetic spectrum. Over time, these III-V semiconductors have remained integral to the development of laser technology, serving also as the foundation of material systems used to create novel laser sources operating in the mid-infrared spectral region, the quantum and interband cascade lasers.

The mid-infrared wavelength region (approximately 2–30 μm) holds particular significance due to the presence of unique absorption spectra of many organic molecules in this region (Fig. 1.1), corresponding to the excitation of these molecules to higher vibrational and rotational states. The distinct absorption spectra of different molecules allows for sensing and spectroscopy.

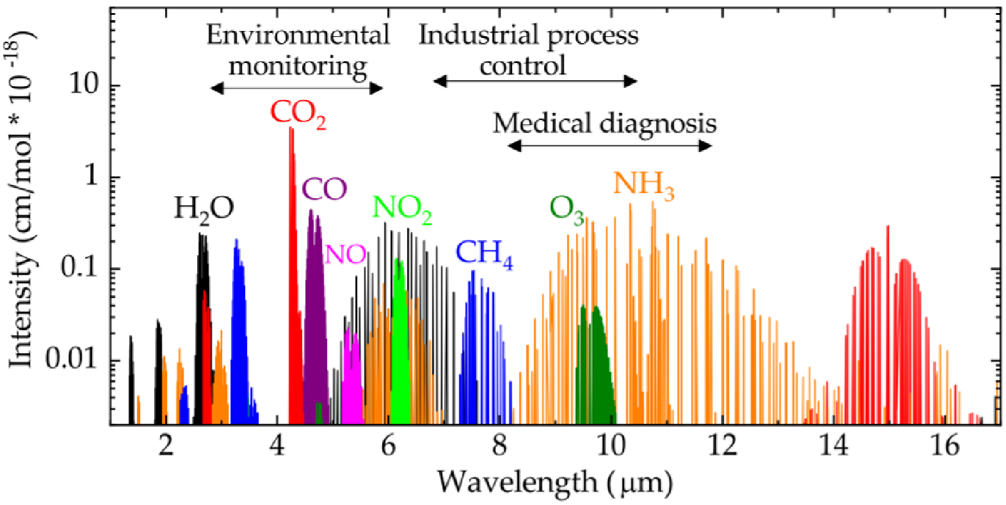

Figure 1.1: Absorption spectra of several selected molecules with strong absorption lines in the mid-infrared spectral region. Taken from [2].

In recent years, there has been a significant progress in the development of photonic integrated circuit (PIC) devices operating in the mid-infrared wavelength region. These devices combine multiple optical components onto a single chip, including light sources, detectors, waveguides, and others, allowing miniaturization, compactness and cost-effectiveness across several fields of application such as gas sensing and environmental monitoring, biomedical diagnosis, and process control. In order to realize these devices, among other prerequisites, reliable lasers operating in the mid-infrared are desired.

In the context of PIC devices, the use of interband cascade lasers (ICLs) together with other semiconductor lasers draws considerable attention due to their stability and also due to the potential compatibility with existing semiconductor fabrication processes and the promise of development of single-chip devices replacing robust and expensive conventional free-space sensing platforms consisting of several external components combined with analyte interaction regions. On top of that, the operating principle of interband cascade devices, discussed in Chapter 2, enables us to achieve relatively high output power with low power consumption, making them ideal candidates for integration into compact, portable and energy-efficient devices.

One of the advantages of ICLs is their narrow bandwidth and potential for adjusting their emission wavelength through the design of their structure. This feature allows us to match the wavelength to specific absorption lines of target molecules in sensing applications with high spectral resolution. However, in certain cases, the need for narrow bandwidth can be outweighed by other considerations, leading to the exploration of alternatives like interband cascade light emitting devices (ICLEDs) as mid-infrared sources.

Instead of the narrow spectral emission of ICLs, ICLEDs produce incoherrent light with a broader emission bandwidth, which can be advantageous in scenarios where precise wavelength tuning or narrow bandwidth is not critical. This characteristic makes them well suited for example for applications where multiple absorption lines need to be probed simultaneously or where the absorption spectrum of the target molecules is broad and complex.

Moreover, ICLEDs offer advantages in terms of fabrication. Although ICLEDs, similarly to ICLs, exploit interband transitions in semiconductor heterostructures to emit light, the primary mechanism of emission is spontaneous emission, rather than stimulated emission and therefore, there is no need for optical feedback, which can lead to reduced complexity in the design of the device and reduced production costs.

However, the fact that spontaneous emission serves as the primary mechanism of emission inevitably leads also to lower power of emitted radiation, making ICLEDs more susceptible to degradation of performance by losses, such as absorption, scattering and non-radiative recombination within the device structure.

That is why significant part of this thesis addresses the different loss mechanisms present in the interband cascade devices influencing their performance and experimental methods used for the measurement and analysis of these losses. The results obtained by these measurement methods can be utilized in optimization of the ICL and ICLED

performance.

Furthermore, in Chapter **??**, the basics of modeling of interband cascade devices are briefly explained and extension of the existing modelling tool developed at TU Wien by implementing the spontaneous emission is presented.

2. Interband cascade devices

This chapter serves as an introduction to the realm of interband cascade devices around which this thesis revolves. Its purpose is to provide context and basic understanding of the operating principles of these devices to lay the theoretical foundation for the following chapters. First, the interband cascade laser (ICL) is introduced as this was the original device utilizing the cascading scheme in combination with interband transitions in semiconductor structures and because its development laid basis for the development of other devices, such as interband cascade photodetectors, frequency combs, vertical-cavity surface-emitting lasers, ring lasers, or light emitting devices (ICLEDs). The section subsequent to the introduction of ICLs is dedicated precisely to ICLEDs and includes literature research on the current state of the art in ICLED design.

2.1 Interband cascade laser

Interband cascade lasers (ICLs) are devices that emit coherent, polarized light in the mid-infrared spectral region. They operate efficiently covering a wide wavelength range spanning from below 2 to above 11 μm in pulsed mode and in continuous wave (cw) mode at room temperature in the range approximately 3–6 μm [3]. They are made of several micrometres thick epitaxially grown heterostructures composed of compound III-V semiconductors, specifically indium arsenide (InAs), gallium antimonide (GaSb), aluminium antimonide (AlSb), and related alloys.

Epitaxial growth

The heterostructures are typically grown by molecular beam epitaxy (MBE), a highly versatile technique for preparing clean, well-defined monocrystalline layers with atomic dimensional control. The MBE growth process involves the reaction of one or more thermal beams of atoms or molecules with a crystalline surface under ultrahigh vacuum (UHV) conditions characterized by a pressure lower than 10^{-7} Pa ($\sim 10^{-10}$ Torr) [4]. The UHV provides a clean surrounding for growth, minimizing the possible contamination of the structures with undesired elements from the residual gas atmosphere.

Due to exact control of the beam fluxes and deposition conditions, controlled growth of films with precise thickness, sharp doping profiles and different chemical compositions changing over a spatial depth of several Ångstroms can be achieved with MBE [5],

allowing fabrication of optical devices tailored to specific needs.

In order to prepare heterostructures suitable for interband cascade lasers, two criteria must be fulfilled: 1) the materials selected for growth must be lattice-matched and 2) they must have suitable properties. One of the epitaxial growth limitations is that the thin films adopt the crystallographic structure related to that of the substrate. That is why, for thin heterostructure layers for high-quality devices, the heterojunctions must be formed by lattice-matched or nearly lattice-matched materials to avoid introducing a significant amount of strain and prevent the formation of defects that would hinder the device's operation. The lattice mismatch should satisfy the condition $\frac{\Delta a}{a} < 10^{-3}$, where $\Delta a = a - a_{\text{epi}}$, which is the difference in the lattice constants of the substrate a and of the epitaxially grown layer a_{epi} [6].

Fig. 2.1a shows lattice constants and band gaps for some of the industrially important and most researched semiconductors. The solid lines joining the binary compounds show the variation in the energy gap as a function of the lattice constant for several ternary solid solution systems. As can be seen in the diagram, the three marked binary III-V semiconductors primarily used for ICL fabrication (InAs, GaSb, and AlSb) create a fitting material system for epitaxial growth since they are nearly lattice-matched (including AlSb/GaSb alloys) with the lattice constant close to 6.1 Å.

Once we have a material system suitable for epitaxial growth, it is also essential to meet the requirement of optoelectronic devices such as ICLs to have specific carrier transport properties, energy gaps and refractive index discontinuities at the heterojunctions that provide carrier and optical confinement. The alignment of the ICL materials bandgaps, illustrated in Fig. 2.1b, demonstrates the fulfilment of this prerequisite. The versatility in combining these materials and their alloys enables the creation of het-

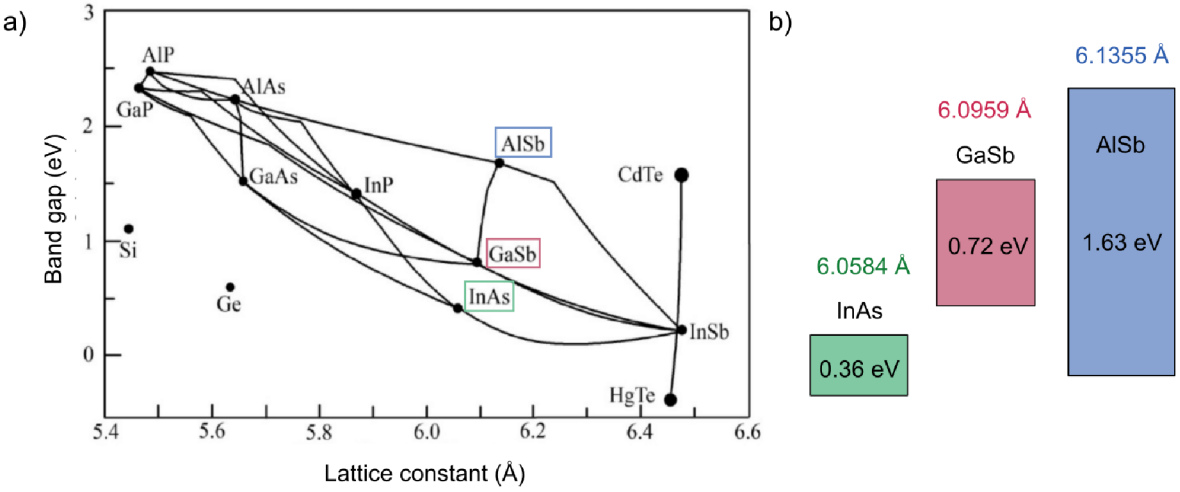

Figure 2.1: a) Energy gap versus lattice constant at 300 K for important semiconductors. The connection lines describe the behaviour of corresponding alloys. Adapted from [7]. b) Band alignment of and lattice constant of materials used in interband cascade laser. Adapted from [8].

erostructure systems with a diverse range of bandgap alignment at heterojunctions, which is a crucial aspect also for facilitating the optical transitions necessary for laser emission.

ICL operation

The lasing action in ICLs is achieved through optical interband transitions between quantized states in specifically designed multiple-quantum well heterostructures. The concept of ICLs was first proposed in 1995 by Rui Q. Yang et al. [10]. They suggested combining the operating principle of type II diode lasers and the cascading scheme. Type II diode lasers (Fig.2.2a) rely on the interband transitions, the recombination of an electron from the conduction band and a hole from the valence band, accompanied by photon emission. Unlike in type I diode lasers, where both the electron and hole are confined within the same material, in type II diode lasers, the electron and hole are spatially separated into different materials, which gives rise to unique optical and electrical properties.

The active region of an ICL where the light is produced consists of several stages with repeating patterns of material layers, creating a system of quantum wells. The interband transitions responsible for generating photons of wavelength defined by the structure occur in each stage. Since the ICL active-region stages are connected in series in contrast to conventional diode lasers, electrons injected into the structure under forward bias are reused and generate an additional photon per stage, as shown in Fig. 2.2. Due to this process, the devices are described as cascading and it leads to high quantum efficiencies (defined by the number of photons generated per electron) and low power consumption.

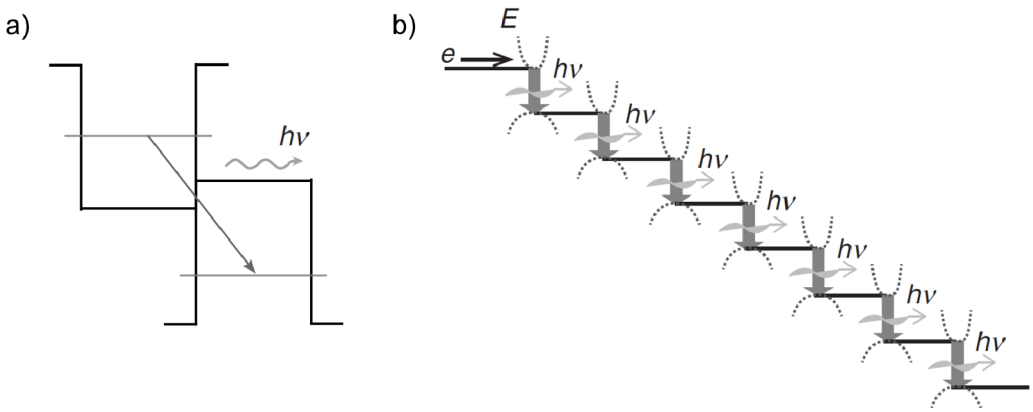

Figure 2.2: a) Illustration depicting the type-II interband transition occurring between the conduction band of the material layer on the left to the valence band of the material on the right. found in diode lasers and ICLs. b) Illustration of the cascading scheme of an ICL under a forward bias. Electron injected into the structure generates a photon with energy $E = h\nu$ (h - Planck constant, ν - frequency) corresponding to the interband transition in each of the stages [9].

The efficient cascading scheme was initially introduced in quantum cascade lasers (QCLs) pioneered by Jerome Faist et al. in 1994 [11]. In contrast to ICLs and traditional diode lasers, QCLs rely on intersubband electron transitions within the conduction band.

The schematic energy band diagram of $1\frac{1}{2}$ stages of an ICL lasing at $\lambda = 3.7\,\mu$m is shown in Fig. 2.3. The figure provides an example of a standard ICL design. Each stage of the active region comprises three sections: multilayer electron and hole injectors and the active quantum wells where the optical transitions occur.

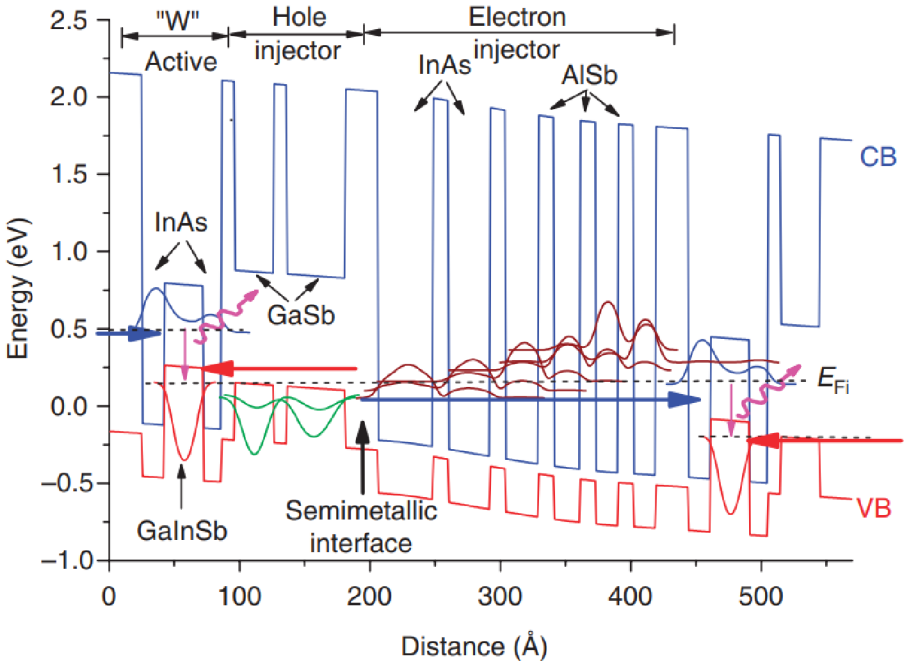

Figure 2.3: Illustrative band diagram of $1\frac{1}{2}$ stages of typical ICL active region. Probability densities for active electron (hole) subbands between which the radiative transition occurs are indicated with blue (red) lines. The probability densities for the injector-electron (hole) subbands where the electrons (holes) are transported through to the active quantum well are indicated with dark red (green) lines. The blue (red) arrows indicate the direction of the electron (hole) motion in the structure. The horizontal dashed lines indicate the position of the quasi-Fermi level in each stage [12].

The optical transition occurs between a conduction band state with its wave function residing mainly in the InAs layers (electron quantum wells), and the valence band state with wave function mainly in the $Ga_{1-x}In_xSb$ layer sandwiched between the InAs layers (hole quantum well). These three layers form the so-called "W" quantum well configuration that maximizes the optical gain by increasing the overlap between electron and hole wavefunctions [13]. The energy separation between the conduction and valence band states can be changed by carefully manipulating the layer thickness. By this bandgap engineering, the emitted wavelength can be tailored for different applications.

In a specific structure, the emission wavelength of an ICL can be further finely tuned by the operating current and temperature. The current injection alters the wavelength through changing the electron and hole populations and the relationship between temperature and wavelength results from the influence of temperature on the band structure and the bandgap.

The state in the conduction band acting as the upper lasing level is populated through the electron injector, and the lower lasing level in the valence band through the hole injector. The electron injector plays a crucial role in maintaining a population inversion that is necessary for achieving the lasing action by quickly depopulating its states. The design of the electron injector consists of several InAs/AlSb quantum wells with specific energy alignment and spatial configuration, facilitating rapid electron transport via a combination of resonant and phonon-assisted tunnelling. The hole injector, comprised of coupled GaSb/AlSb quantum wells, serves a similar purpose. On top of that, it prevents electron tunnelling leakage from the active electron wells to the electron injector in the next stage [14].

Although only electrons are injected into and removed from the ICL, both electrons and holes are present in each stage of the ICL's active region. This is the key feature in any interband cascade device allowing the cascading and it is provided by the semi-metallic interface at the boundary between the electron and hole injectors. This interface acts as an internal generator of charge carriers, as illustrated in Fig. 2.4. The band alignment of the InAs/GaSb so-called broken-gap heterojunction is characterized by the bottom of the conduction band in InAs lying approximately 0.2 eV below the top of the valence band in GaSb at room temperature [15]. This unusual band align-

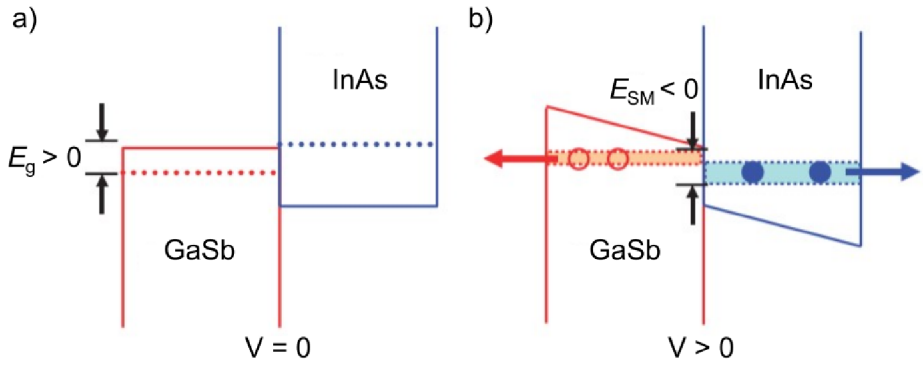

Figure 2.4: The energy alignment for adjacent InAs and GaSb quantum wells in equilibrium (a) and under bias (b). The solid blue and red lines indicate the conduction and valence-band edges, respectively. In the absence of a bias, quantum confinement leads to an energy gap E_g between the lowest conduction and highest valence band states (blue and red dotted lines, respectively), whereas under bias a semi-metallic overlap E_{SM} is imposed that leads to the generation of electron and hole densities, represented by the solid blue and open red circles, respectively. The applied field causes carriers to flow away from the interface (arrows). Adapted from [12].

ment causes the junction to exhibit semi-metallic properties when an external field is applied. Without an applied external field, electrons and holes are localized on opposite sides of the interface. However, when an external field is applied, the bottom conduction subband is lowered with respect to the top valence subband, producing a voltage-dependent band overlap of $E_{\mathrm{SM}}(\mathrm{V})$. At typical operating voltages, this overlap is $\approx 100\,\mathrm{meV}$ [14]. The induced semi-metallic overlap E_{SM} generates equal electron and hole densities. The applied field also causes both types of carriers to flow away from the interface towards their respective active quantum wells.

It is worth noting, that in the absence of external field, the active stages of an ICL can function also as an detector without requiring any modifications. This is because incident photons having energy corresponding or higher than that of the interband transition induce photocurrent that flows in the opposite direction to that which produces gain under forward bias. The electrons get lifted to the conduction band and then slowly decay into the next step due to the defined cascading structure.

Laser cavity

The radiative recombination in the active region supported by the effective carrier transport itself is insufficient to achieve lasing. To sustain the lasing process by ampli-

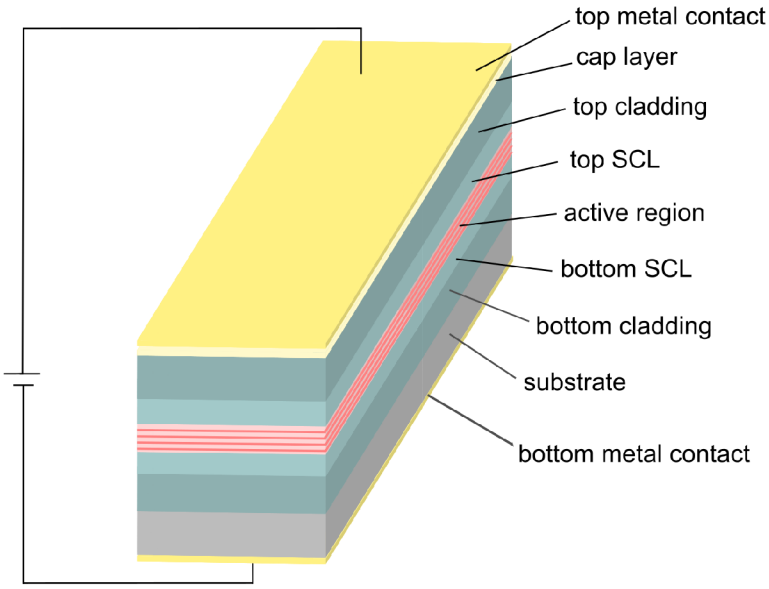

Figure 2.5: Schematic layering of an ICL structure. The primary regions are the active stages, top and bottom separate confinement layers (SCL), and top and bottom superlattice optical cladding layers, grown on a suitable substrate and forming the waveguiding structure. The cap layer ensures low-resistance electrical contact between the metal and semiconductor, and the top and bottom metal contacts allow the application of an external field providing the current injection. Note that the dimension proportions in the drawing are out of scale compared to real situations.

fying the light within the gain medium, it is necessary to incorporate optical feedback and create a laser cavity and an efficient waveguiding structure, which confine the electromagnetic field into well-defined optical modes.

A simplified schematic structure of a whole ICL is depicted in Fig. 2.5. The waveguiding structure grown on the substrate comprises following basic building blocks: the active region (usually 5 to 12 stages), surrounded by separate-confinement layers (SCL) and superlattice optical cladding.

Generally, the laser waveguide needs to guarantee sufficient overlap of the propagating mode with the active region while minimizing internal losses. The confinement of the mode and the sufficient overlap with the active region is typically ensured by creating a refractive index contrast between the active region and the cladding layers (Fig. 2.6). The thick superlattice top and bottom cladding have significantly lower refractive index than that of the active region, leading to the confinement within by total internal reflection and separation of the optical mode from the highly doped cap layer and the substrate to avoid free carrier absorption (discussed in the following chapter) and mode leakage to the high refractive index substrate. However, the losses in the cladding are relatively high, which is the reason for incorporating the SCL layers, which have higher refractive index than both the cladding and the active region, but the doping and related carrier-absorption-induced losses are much lower. Hence, although a large proportion of the mode is confined in these layers, they lead to improvement of the device efficiency by effectively reducing the waveguide losses [16].

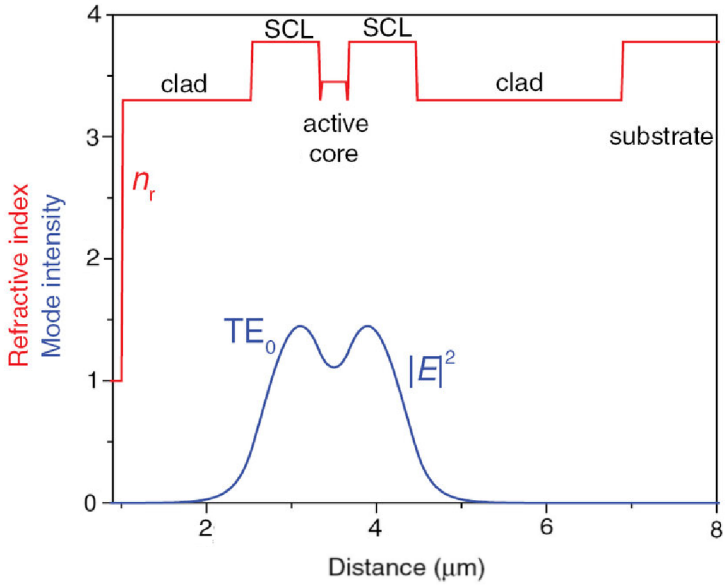

Figure 2.6: Profiles of the real part of the effective refractive index and optical intensity for the fundamental TE mode of a slab ICL waveguide with a 7-stage active core and 800 nm-thick GaSb SCLs used as an illustration of the mode confinement and refractive index contrast in the ICL waveguide. Taken from [17].

The waveguiding structure confines the optical mode in the growth (vertical) direction. Lateral confinement is most commonly achieved by etching the semiconductor layers to create a ridge geometry. In the simplest cases, the optical feedback is obtained using the cleaved facets to form a Fabry-Pérot resonator. The facets formed by cleaving the material along the crystallographic direction create a high-quality semiconductor-air interface. Due to the refractive index discontinuity at these interfaces, the facets act as partially reflecting mirrors. If emission from a single facet is preferential, the facets can be coated to modify their reflectivities. The out-coupled light at both sides of the ICL waveguide is quantified by the mirror losses given by

$$\alpha_{\mathrm{m}} = \frac{1}{2L} \ln\left(\frac{1}{R_1 R_2}\right), \tag{2.1}$$

where L is the cavity length and R_1, R_2 are the two mirror reflectivities.

The condition to reach the lasing threshold in ICLs as well as in other lasers is quite simple. In order to sustain the lasing, the losses from the mirrors α_{m} and internal losses α_{i} stemming from the interaction of the mode with the waveguide material system need to be overcome by the optical gain. Hence the gain at threshold g_{th} given by material gain and the modal overlap of the propagating light with the gain region, exactly compensates the losses:

$$g_{\mathrm{th}} = \alpha_{\mathrm{m}} + \alpha_{\mathrm{i}}. \tag{2.2}$$

This equation separates the losses in a laser into localized losses due to the mirrors that can be affected by treatment, and distributed losses that cannot be influenced externally, only by the design and fabrication. Chapter 2 focuses on the origin of the internal losses in interband cascade devices that are essential for understanding their limitations.

The lasing threshold is usually characterized by another critical parameter which is the threshold current density, J_{th}, directly related to g_{th}. Lowering J_{th} is crucial for efficient laser operation, as it determines the minimum current required to initiate lasing. Lower J_{th} results in reduced power consumption, and improved thermal management.

2.2 Interband cascade light emitting device

It is conventional for LED and diode laser designs to utilize multiple quantum wells (MQWs) to improve their performance. This strategy is employed because MQWs can significantly enhance the internal quantum efficiency of LEDs by increasing the probability of radiative recombination through carrier confinement.

However, a pronounced decrease in output power at room temperature is still evident in the current state-of-the-art mid-infrared LEDs. Achieving efficient mid-infrared LED sources emitting with power greater than 1 mW in the spectral region above 2 μm remains a challenge. And despite the advantages of LEDs, such as low power consump-

tion and high modulation rate, there are still relatively few examples of commercial LED-based mid-infrared instruments due to the technical limitations [18]. Interband cascade light emitting devices (ICLEDs) provide one way to overcome these limitations. They use the same active stages that produce optical gain in an ICL without the optical feedback to generate light through spontaneous emission. Therefore, they benefit from the expertise developed for cascade active regions in ICL structures.

In contrast to ridge ICLs, a typical ICLED uses a vertical emission architecture similar to the one displayed in Fig. 2.7. The ICLEDs are typically mounted epitaxial-side-down, with the light extracted through the substrate. To date, ICLEDs with 15-22 active region stages have been reported.

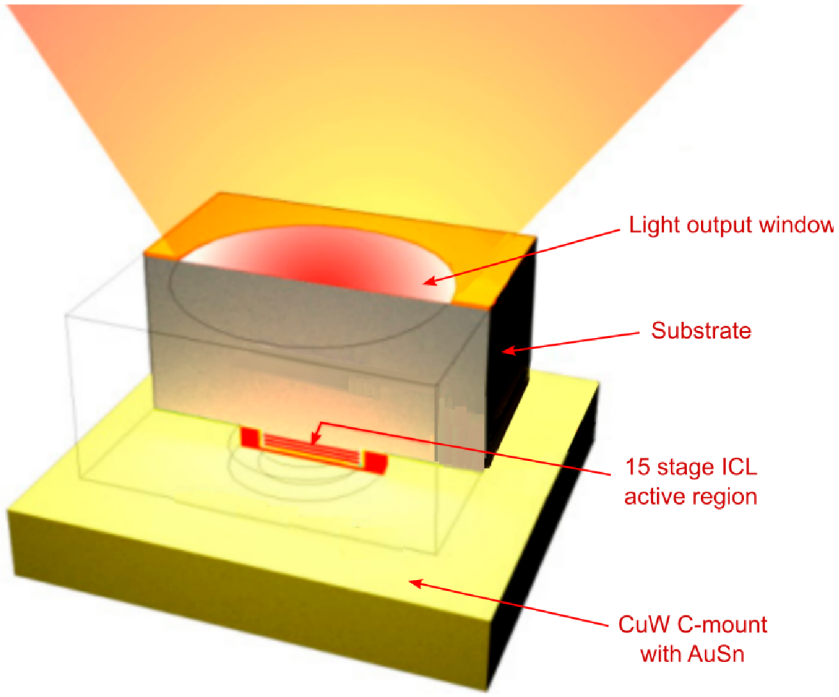

Figure 2.7: Schematic of a typical ICLED architecture. The epitaxial-side-down mounted device emits through an annular bottom contact on the substrate side. Adapted from [14].

One of the first times evidence of interband electroluminescence emitted from the surface of a type-II cascading structure in the 5–8 μm spectral range was reported in 1997 [19]. The structure comprised 15 stages, and the achieved output optical power reached up to 700 nW.

Several years later, investigations by N. Das et al. showed in various papers that treatments of the output surface could enhance emission efficiency and output power since, although ICLEDs can achieve high internal quantum efficiencies, a low wall-plug efficiency is obtained due to low optical extraction. The optical extraction from an LED usually is very inefficient due to total internal reflection leading to out-coupling from the untreated substrate to be less than 4 % [14]. By thinning out a GaSb substrate

to 20 μm and patterning the output surface of the substrate with square grating in [20], the emission from an 18-stage ICLED with peak wavelength at 3.8 μm was increased from 40 μW per pixel to 400 μW at room temperature. They also found substantial enhancement of the out-coupling by deposition of 20 nm of Au on the output surface to provide a localized surface plasmon resonance [21].

C. S. Kim et al. [22] further reported improvement in the performance of 22-stage devices by grouping the stages into four groups positioned at antinodes of the internally reflected optical field, as shown in Fig. 2.8. By grouping the stages, the IR radiation interferes constructively with itself when reflected at small angles from the top metal contact of the epitaxial-side-down mounted device, doubling the maximum output power. With this approach, an ICLED with peak wavelength 3.1 µm emitted up to 2.9 mW of cw power at 25 °C, with a maximum wall-plug efficiency of 0.4 %.

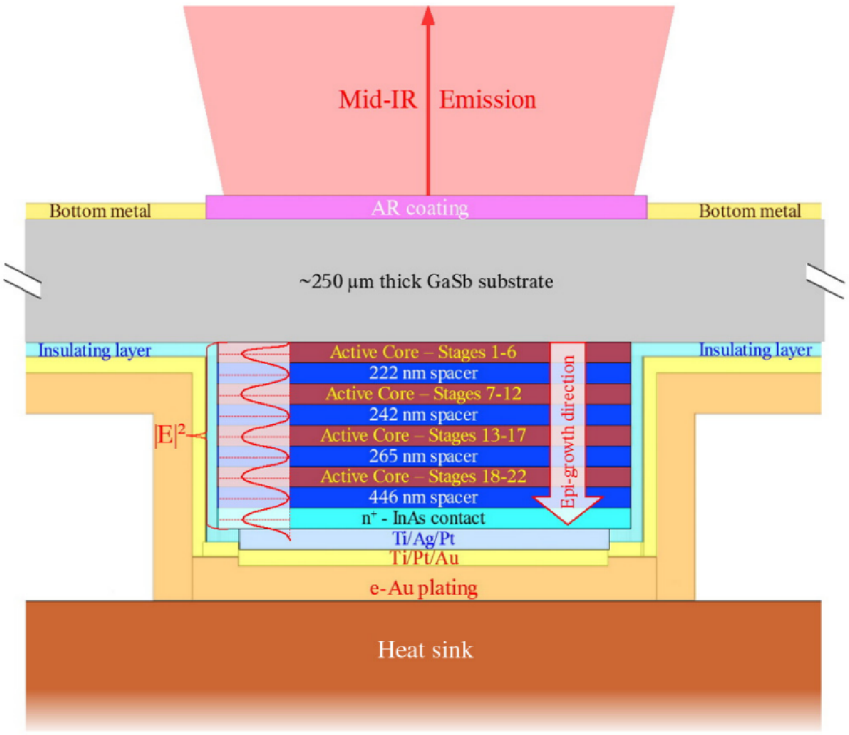

Figure 2.8: Schematic of the epi-side-down mounted ICLED mesa with 22 active stages split into four groups positioned at antinodes of the optical field reflected from the metal contact. The optical intensity profile $|E|^2$ is depicted by the red line next to the schematic of the active region heterostructure [22].

The grouping of stages has been further explored by, for example, Nanoplus. Utilizing this technique, they managed to obtain up to 5.1 mW of CW output at peak wavelength 3.7 µm with 640 μm squared mesa while also achieving the highest wall-plug efficiency of 0.7 % ever reported for room temperature [23]. Note that the wall-plug efficiency of any mid-IR LED decreases markedly with increasing drive current and output power due to the rapidly increasing Auger recombination rates (described in

Chapter 3) with injected carriers, leading to lower radiative efficiency.

Another technique to enhance the out-coupling in ICLEDs is to add top and bottom mirrors as in vertical-cavity surface-emitting lasers (VCSELs) but operate below the gain threshold to form a resonant cavity LED. This has the effect of enhancing the emission rate due to a higher optical field at the cavity's antinodes while improving the output's directionality and narrowing the emission bandwidth [24]. While ICLEDs adopting the VCSEL architecture lead to narrower bandwidths, it is also possible to broaden the ICLED bandwidth by cascading independently designed stages with different bandgaps [14].

Growth of ICLEDs on mismatched silicon substrates was also reported [25]. Despite the lattice mismatch and additional strain caused by differences in the thermal expansion coefficients of Si and III-V semiconductors, improved radiance was reported due to the much higher transparency of silicon in the mid-infrared region. On top of that, dissipation via the substrate allowed devices on Si to operate with much higher current densities. The growth on Si opens up the possibility of the heterogeneous integration of ICLEDs with widespread low-cost CMOS technology.

As was already mentioned in the introduction, ICLEDs hold potential in several fields of application. They were already successfully utilized for the detection of methane [26] and NO_2 [27] and suggested as a potential source for IR scene projection arrays [14].

3. Losses in interband cascade devices

The gain and loss mechanisms in semiconductor lasers are largely determined by the band structure of the laser's active region and the surrounding material layers. Dominant loss processes vary significantly with emission wavelength and the material composition of the laser structure [28].

The internal losses α_i in interband cascade devices stem from various mechanisms within the device structure. These losses arise from similar mechanisms as in other semiconductor lasers and diodes.

Internal losses include both non-radiative processes and absorption losses. Absorption losses reduce the number of already generated photons within the device, while non-radiative losses prevent photon emission. Non-radiative losses are primarily attributed to carrier recombination processes such as Auger recombination and Shockley-Read-Hall recombination, carrier leakage and resistive losses. In this chapter, non-radiative recombination and different types of absorption are reviewed.

3.1 Non-radiative recombination

In the thermal equilibrium, the product of the electron concentration n and hole concentration p is constant and known as intrinsic carrier concentration:

$$n_i^2 = np. \tag{3.1}$$

However, an applied external field introduces excess charge carrier in the semiconductor heterostructure and generates a non-equilibrium situation ($np > n_i^2$). Recombination processes between electrons and holes tend to restore the equilibrium state [29].

Three fundamental mechanisms of electron-hole recombination can be distinguished and are depicted in Fig. 3.1. The radiative recombination contributes to photon emission, and the non-radiative recombination processes, Shockley-Read-Hall and Auger, contribute to losses.

Shockley-Read-Hall Recombination

Shockley-Read-Hall non-radiative recombination, often called defect or trap-assisted, was first observed in a germanium crystal and mathematically described in 1952 [30].

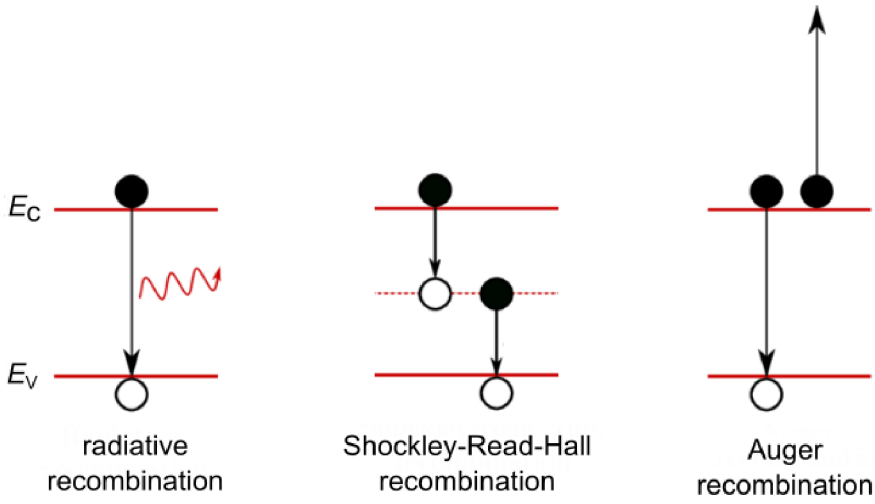

Figure 3.1: Schematic illustration of the recombination mechanisms present in semiconductor lasers. The solid red lines represent the conduction band (E_c) and valence band (E_v) states. Radiative recombination (left) results in photon emission. Shockley-Read-Hall recombination (centre) is relaxation via defect states or traps (dotted red line) within the semiconductor bandgap. Auger recombination (right) involves an additional charge carrier which is excited by absorbing the energy released by the recombination process.

Defects and impurities in the semiconductor crystal lattice create energy states within the bandgap, also called trap levels, that act as recombination centres. Electrons and holes can recombine through these defect states without emitting photons. The two-step recombination process involves the relaxation of electrons to the defect level followed by relaxation to the valence band, annihilating a hole in the process [31].

The SRH recombination rate R_{SRH} is given by

$$R_{\mathrm{SRH}} = \frac{np - n_{\mathrm{i}}^2}{\tau_{\mathrm{h0}}(n + n_0) + \tau_{\mathrm{e0}}(p + p_0)}, \tag{3.2}$$

where τ_{h0} and τ_{h0} are carrier lifetimes for holes and electrons, respectively, whose values depend on the type of trap and the density of traps [32]. The parameters n_0 and p_0 introduce the dependency of the rate on the trapping energy level E_{t} as

$$n_0 = n_{\mathrm{i}} \exp\left(\frac{E_{\mathrm{t}} - E_{\mathrm{i}}}{kT}\right) \tag{3.3}$$

and

$$p_0 = n_{\mathrm{i}} \exp\left(\frac{E_{\mathrm{i}} - E_{\mathrm{t}}}{kT}\right), \tag{3.4}$$

where E_{i} denotes the middle of the bandgap. These expressions show that impurities that introduce energy levels near the midgap are very effective recombination centres.

If the injected carrier densities are much larger than intrinsic carrier densities, the

recombination rate simplifies to $R_{\mathrm{SRH}} \approx n/(\tau_{\mathrm{e0}} + \tau_{\mathrm{h0}})$, yielding a linear dependence on injected carrier density.

This type of recombination is structure-sensitive and particularly prevalent in materials with high levels of impurities or structural imperfection since the recombination rate is directly proportional to the density of traps. Thus, high-quality heterostructures grown by MBE are desired to suppress this type of non-radiative recombination.

Auger recombination

Auger recombination is a three-carrier process involving either two electrons and one hole (*eeh* process) or two holes and one electron (*hhe* process). When electrons and holes recombine, their energy is transferred to a third carrier, which is then excited to a higher energy state instead of emitting photons. The excited carrier eventually relaxes back to the edge of the respective band and loses its excess energy as heat through phonon interactions.

Fig. 3.2 shows four different *eeh* Auger processes facilitated by direct/indirect and intraband/interband carrier transitions. Inversely, similar processes occur for the *hhe* Auger recombination. All of these processes need to abide by the momentum and energy conservation.

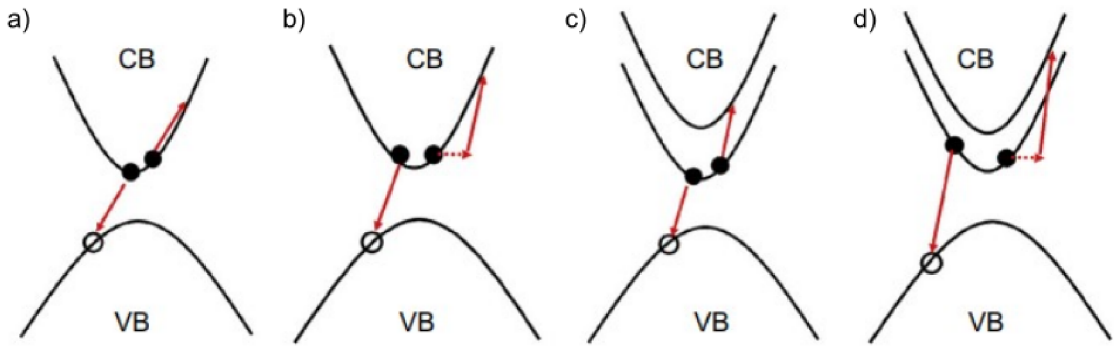

Figure 3.2: Schematics of different Auger recombination processes: a) direct intraband, b) indirect intraband, c) direct interband, and d) indirect interband. The solid lines represent the energy dispersion $E(k)$ of the conduction band (CB) and valence band (VB) subbands. The solid arrows are momentum transferred from electron-hole recombination, while the dashed arrows represent a scattering mechanism, such as alloy scatttering or electron-phonon coupling. Adapted from [33].

Because this process is based on the ability of the charge carriers to exchange energy, the probability of Auger recombination increases with a higher carrier concentration. For an *hhe* process, we expect the reaction mechanism to be proportional to p^2n and *eeh* process proportional to n^2p. Hence the Auger recombination rate R_{A} is given by

$$R_{\mathrm{A}} = C_{\mathrm{n}} n^2 p + C_{\mathrm{p}} p^2 n, \tag{3.5}$$

where C_n and C_p are the capture probability coefficients when the third carrier is electron or hole, respectively [34]. If the hole and electron concentrations are assumed to be equal, the Auger rate is dependent on the cubed carrier density $R_\mathrm{A} \propto n^3$.

Under the assumption of parabolic bands and low carrier densities, the carriers can be considered to follow the Boltzmann distribution, yielding the Auger capture coefficients to be

$$C_\mathrm{n,p} \propto \exp\left(-\frac{E_\mathrm{a}}{kT}\right). \tag{3.6}$$

E_a is the activation energy, which depends on the in-plane masses of the carriers involved in the recombination and is linearly dependent on the bandgap energy E_g [35]. The dependence of the rate on the bandgap energy translates to dependence on the wavelength. If the bandgap is smaller, corresponding to a longer wavelength, the activation energy is also smaller, making the recombination process more probable. Additionally, according to Eq. 3.6, higher temperature also leads to increased prominence of the Auger recombination.

More accurate descriptions of the Auger process can be derived by considering Fermi-Dirac statistics and the non-parabolicity of the conduction and valence bands. Moreover, the situation in semiconductor lasers is more complex due to the formation of quantum wells and carrier confinement, which significantly alter the carrier dynamics and recombination processes. Experimental values of the Auger coefficient in such structures can vary widely depending on material composition, doping levels, and temperature, and sophisticated measurement techniques are often required for the coefficients to be accurately determined.

3.2 Absorption

Absorption in semiconductor devices results in loss of the optical signal propagating through the device, or in other words, reduction of the number of photons generated through radiative recombination. Depending on the material, doping, temperature, and the wavelength range of interest, various absorption mechanisms in semiconductor materials dominate to different degrees. The most relevant absorption mechanisms in III-V semiconductors are free carrier absorption, inter-valence band absorption and inter-valley conduction band absorption. These absorption mechanisms are briefly addressed following [36]. The general description of inter-valence band absorption is then followed by description of valence intersubband absorption in the hole quantum well of the W quantum well system utilized in interband cascade devices, which is subject of measurements presented in last section of Chapter 4.

Free carrier absorption

The term "free carriers" refers to the electrons in the conduction band and the holes in the valence band that are free to move and contribute to electrical conduction. Free

carrier absorption is a phenomenon in which a material absorbs a photon, resulting in the excitation of an already excited free electron or hole to a higher unoccupied energy level within the conduction or valence band, respectively. Generally, free carrier absorption can only occur accompanied by an additional scattering event to fulfil momentum conservation [35].

The absorption coefficient characterizing the free carrier absorption, α_{FCA}, is conventionally defined following the classical Drude model of the charge carrier transport as:

$$\alpha_{\mathrm{FCA}} = \left(\frac{e^3}{4\pi^2 c^3 m_0^2 \epsilon_0}\right)\left(\frac{1}{n(m^*/m_0)^2}\right)\left(\frac{\lambda^2}{\mu}\right) n_{\mathrm{e,p}} = s\lambda^2 n_{\mathrm{e,p}}, \tag{3.7}$$

where n is the refractive index, m* is the effective mass of the carrier, μ is the mobility, $n_{e,p}$ is the free carrier (electron/hole) concentration, and λ is the incident wavelength. We can see that according to the classical approach, the absorption coefficient should exhibit linear dependence on the free carrier concentration and quadratic dependence on the wavelength.

However, more precise calculations applying the quantum mechanical principles show that the exponent of the wavelength yields different values for different dominant scattering mechanisms encompassing free carrier absorption. The absorption coefficient for electrons can then be expressed as a weighted sum:

$$\alpha_{\mathrm{FCA}} = s(A\lambda^{1.5} + B\lambda^{2.5} + A\lambda^3). \tag{3.8}$$

The dependency on $\lambda^{1.5}$ represents carrier collision with the lattice resulting in scattering by acoustic phonons, $\lambda^{2.5}$ represents scattering due to optical phonons, and λ^3 scattering by ionized impurities. A, B and C are fitting parameters.

To further simplify the expression and reduce fitting parameters to two, the following equation can be used:

$$\alpha_{\mathrm{FCA}} = K_{\mathrm{FCA}}\lambda^m. \tag{3.9}$$

The constant K_{FCA} depends directly on the doping of the semiconductor and also takes into account any dependence of the mobility on doping.

Inter-valley conduction band electron absorption

An inter-valley conduction band absorption involves the transition of an electron between local energy minima (valleys) of one conduction subband at different k-points. Both acoustic and optical phonons can cause the phonon-assisted electron transitions.

The dependence of the absorption coefficient characterizing this process within the conduction band, α_{CB}, on the energy (wavelength) of the incident photons, can be expressed as

$$\alpha_{\mathrm{CB}} = K_{\mathrm{CBV}}\left(\hbar\omega - E_0\right)^{1/2} \approx K_{\mathrm{CBV}}\left(\frac{1.24}{\lambda} - E_0\right)^{1/2}, \tag{3.10}$$

where K_{CBV} is the fitting parameter dependent on carrier concentration, $\hbar\omega$ is the

photon energy and E_0 is threshold energy for the inter-valley transitions given by

$$E_0 = \Delta E + E_\mathrm{p} - E_\mathrm{F}. \tag{3.11}$$

This term includes the energy separation between the valleys ΔE, the energy of the involved phonon E_p and the position of the Fermi level E_F.

The decrease in the absorption coefficient with increasing wavelength leads to the inter-valley conduction band absorption being the governing mechanism of the total internal absorption only at lower wavelengths.

Inter-valence band absorption

The valence band in typical semiconductors comprise light-hole (LH), heavy-hole (HH) and split-off (SO) bands. Transitions of carriers within these bands are allowed, which gives rise to inter-valence band absorption. At elevated temperatures or in heavily doped p-type, that have a Fermi energy below the valence band edge, transitions are possible from the LH band to the HH band or from the SO band to the HH or LH bands [37].

The theoretical description of inter-valence band absorption is much more complex than in the previous cases. Following the Kane model describing the III-V semiconductor band structure, the derived absorption coefficients for different inter-valence band absorption processes show linear dependency on the carrier density. The obtained expressions also facilitate the different effective masses of the respective bands and the frequency of the incident radiation.

When designing a laser, resonances between the lasing wavelength and the split-off energy E_SO separating the SO band from LH and HH bands at the Γ-point ($k = 0$) of the band structure should be avoided since the absorption depends on the carrier density, which is highest at the Γ-point. However, the absorption due to transition from the SO band at Γ-point occurs only in materials where $E_\mathrm{SO} < E_\mathrm{g}$. This does not apply, for example, in GaSb, and the inter-valance band comes mainly from LH-HH transitions.

The inter-valence band absorption is believed to have a more significant effect at higher wavelengths as it has been previously considered to be a possible cause of the temperature sensitivity of threshold currents in longer-wavelength semiconductor lasers [38].

Valence intersubband absorption in the W quantum well

The ICL performance "sweet spot" lies in the 3–4 μm range, where the performance is considered optimized since the threshold current and power densities appear to be approaching theoretical limits [17]. Outside this wavelength range, ICL performance degrades, and it has proven highly challenging to extend the cw operation at room temperature toward longer wavelengths. The same can be said about other interband

cascade devices since their operation and limitations are governed by the same underlying mechanisms, especially in the active region.

In the longer-wavelength devices, the degradation of ICL performance is typically attributed to the rapid wavelength scaling of the multi-carrier Auger recombination and the free-carrier absorption, along with the reduced overlap of the electron and hole wavefunctions in the W quantum well (W-QW) [17]. However, very recently, H. Knötig et al. [39] recognized resonant intersubband absorption in the valence band to be causing the performance drop in ICLs operating in the 4–5 μm region and presented a solution to overcome it. This research, supported by simulations and experiment, found a direct dependency of the valence intersubband absorption on the thickness of the $Ga_{1-x}In_xSb$ hole quantum well (h-QW) in the W-QW system and presented a way to reduce the unwanted absorption.

Most of the ICL designs presented in the literature, predominantly employing h-QWs with the thickness of 3 nm, always exhibited performance degradation at longer wavelengths. Knötig et al. suggested that a more careful design of the active W-QW can overcome this negative trend. Some of the results of the numerical simulations conducted in their work are shown in Fig. 3.3. The electronic band structure at the Γ-point of a specific W-QW design with emission wavelength of 4.6 μm and 3 nm thick $Ga_{0.65}In_{0.35}Sb$ h-QW is depicted in Fig. 3.3a. The red and black subbands have dominant heavy-hole and light-hole band contributions, respectively. The red arrow in the plot in Fig. 3.3b, depicting the valence band structure in dependence on the in-plane wave vector for the same design, indicates a possible transition between those subbands. For the specific design, this transition matches the emission wavelength of the device.

To obtain a more detailed picture, they simulated absorption with varying h-QW thickness. The simulation results are shown in Fig. 3.3c. As can be seen from the absorption map, following the dashed white line representing an h-QW thickness of 3 nm corresponding with the previously mentioned design, a pronounced absorption does, in fact, occur at the emission wavelength 4.6 μm, undeniably confirming the presence of intersubband absorption in this device. Note that the nature of the absorption mechanism is, however, nontrivial as the two solid lines in this plot corresponding to the transition energies at the Γ-point between the calculated subbands do not fit the absorption features completely since dominant absorption can also occur at nonzero in-plane k values.

The data in Fig. 3.3 were calculated for a Fermi level set to the uppermost valence subband at $k = 0$ and for a temperature of 300 K. Assuming the thermal distribution of carriers with a fixed Fermi level, the intersubband absorption is expected to increase with temperature, as it is expected to depend on the hole density. By this reasoning, one would also expect that the resonant absorption would depend on the voltage applied to the devices, as higher voltage introduces more carriers and, hence, a higher probability of intersubband transitions. This voltage dependency is experimentally proven in the following chapter.

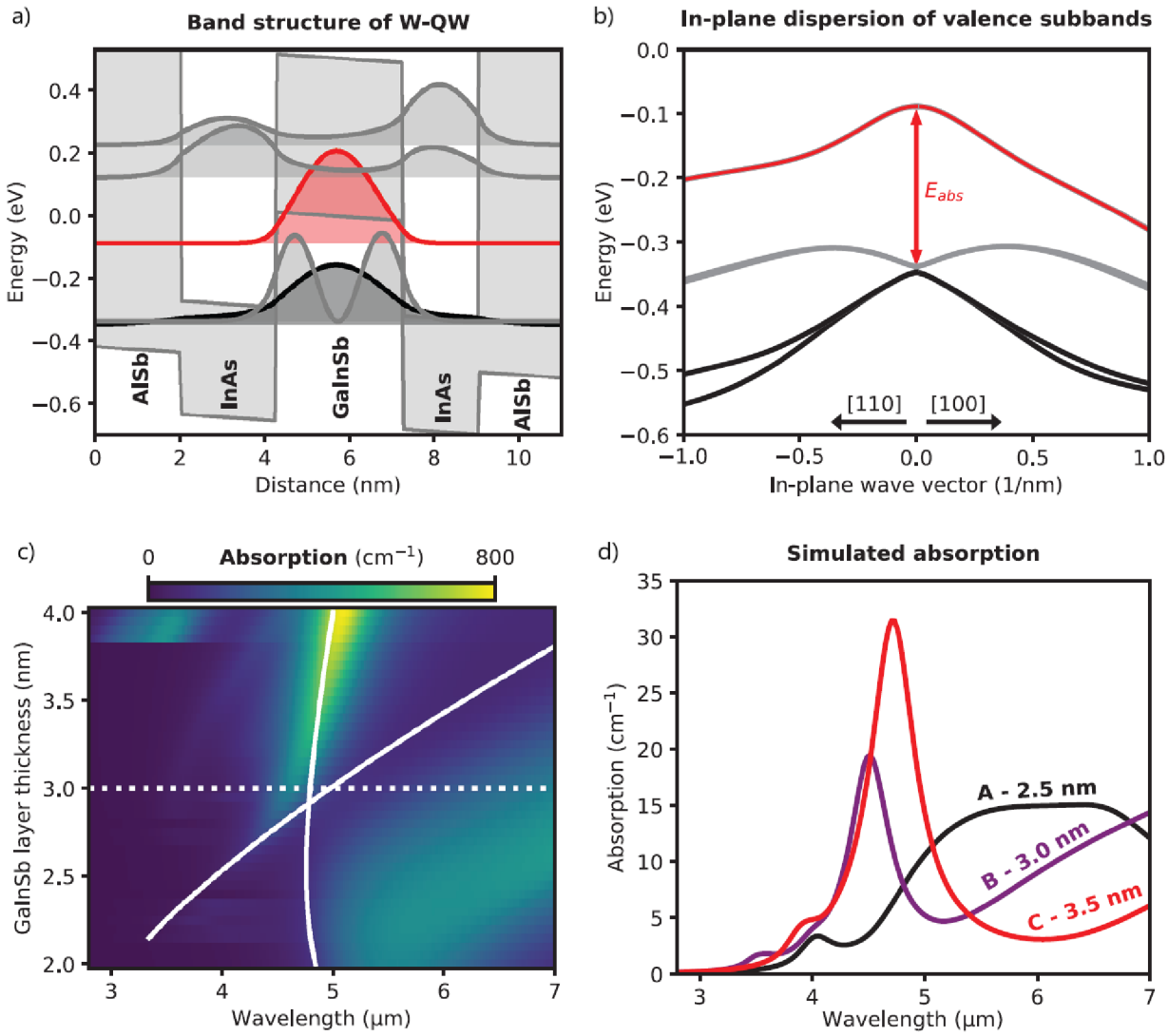

Figure 3.3: a) Simulation of a W quantum well band structure of an ICL with 3 nm thick $Ga_{0.65}In_{0.35}Sb$ h-QW emitting at $\lambda = 4.7\,\mu m$ calculated at the Γ-point. Probability densities of the heavy hole-like and the light hole-like subbands are plotted in red and black, respectively. b) Relevant subbands for the intersubband transitions plotted in dependence on the in-plane wave vector k for the same ICL design as in (a). A possible intersubband transition is indicated by the red arrow. c) Calculated absorption in the valence band depending on the $Ga_{0.65}In_{0.35}Sb$ layer thickness and wavelength. The two solid white lines indicate the wavelengths corresponding to the energy difference at the Γ-point between the calculated subbands (red-black and red-gray). The dashed line indicates the h-QW thickness of 3 nm. d) Dependence of the absorption on wavelength for three structures emitting at $\lambda = 4.35\,\mu m$ with $Ga_{0.6}In_{0.4}Sb$ h-QW calculated for different h-QW thicknesses. The Fermi level was fixed to the uppermost valence subband at $k = 0$ and a temperature of 300 K was used for the simulations [39].

4. Methods and results

4.1 Spectroscopic methods

4.1.1 Fourier transform infrared spectroscopy

Fourier transform infrared spectroscopy allows, like classical spectroscopy, to obtain the transmission spectrum of the sample under investigation. For the measurements conducted in this thesis, Burker VERTEX 70v FTIR Spectrometer located at TU Wien was used. The spectrometer provides the possibility to acquire a complete far- and mid-infrared spectrum from $6000\,\mathrm{cm}^{-1}$ to $50\,\mathrm{cm}^{-1}$ in a single step measurement corresponding to the wavelength range $1.66\,\mu$m to $20\,\mu$m. (Here, the wavenumber is defined as $\tilde{\nu} = 1/\lambda$). A simplified scheme of the optical setup in this FTIR Spectrometer is shown in Fig. 4.1. The setup of the light source, interferometer, sample compartment, and a detector.

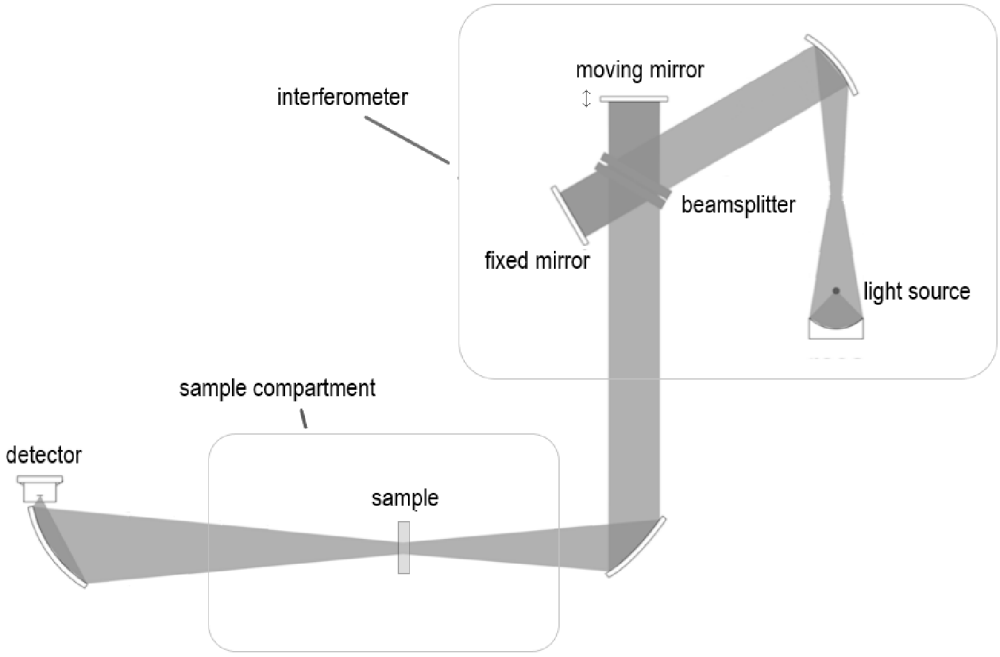

Figure 4.1: Schematic illustration of the optical path beam in the Bruker FTIR spectrometer setup configuration used for the measurements.

The measured samples are mounted on a holder in evacuable compartment with the vacuum in reaching 0.2 hPa (150 mTorr). The vacuum environment helps to eradicate the strong absorption of water vapor and CO2 present in the mid-infrared spectral region.

The light beam from the broadband infrared light source, consisting of a globar (a glowing silicon carbide rod), first passes through a Michelson interferometer, where the light is collimated and than directed to a beam splitter. The beam splitter splits beam into two, one beam is refracted towards the fixed mirror and one transmitted towards the moving mirror. Light is reflected from the two mirrors back to the beam splitter and some fraction of the original light passes into the sample compartment. There, the light is focused on the sample.

The movable mirror serves to change the difference in the optical paths of the interfering beams refleted from the mirrors δ. If the difference in the optical paths is $\delta = n\lambda$, where λ is the wavelength of the light coming from the source, the light interferes constructively at the interferometer output. For $\delta = (n + \frac{1}{2})\lambda$, the light interferes destructively. Thus, in general, for monochromatic light, the intensity at the output of the interferometer can be described as [40]

$$I(\lambda, \delta) = \frac{1}{2} I_0(\lambda) + \frac{1}{2} I_0(\lambda) \cos \frac{2\pi\delta}{\lambda}, \tag{4.1}$$

where I_0 is the intensity of the incoming light. The first term in Eq. 4.1 is constant, unlike the second term that changes with δ. An interferogram is a plot of this intensity as a function of δ showing the interference pattern produced by the interferometer. In the following text, we consider only the second term, which represents the oscillatory part of the interferogram and is responsible for the interference pattern observed.

If there is a broad-spectrum source at the input of the interferometer, the intensity at the output will be:

$$I(\delta) = \int_{-\infty}^{+\infty} \frac{1}{2} I_0(\lambda) \cos \frac{2\pi\delta}{\lambda} \, d\lambda \ . \tag{4.2}$$

In the experiment, this signal is then altered by the interaction with the sample quantified as the transmittance $T(\lambda)$. The transmission through a material system changes the interferogram in the following way:

$$I(\delta) = \int_{-\infty}^{+\infty} \frac{1}{2} I_0(\lambda) T(\lambda) \cos \frac{2\pi\delta}{\lambda} \, d\lambda \ . \tag{4.3}$$

During the measurement, the interferometer mirror is moved and the intensity is recorded by the detector, in our case a HgCdTe (MCT) photodetector cooled to liquid nitrogen temperature. To retrieve a spectral dependence of the intensity after

transmission, I_{T}, the obtained signal $I(\delta)$ is processed using the Fourier transform [40]

$$I_{\mathrm{T}} = I_0(\lambda)T(\lambda) = \int_{-\infty}^{+\infty} 2I(\delta)e^{\frac{-i2\pi\delta}{\lambda}}d\delta. \tag{4.4}$$

Since the interferogram in an actual experiment cannot be measured over an infinite interval, the Fourier transform results in the convolution of the spectrum with a window function corresponding to the measured interval. To suppress this artifact, the interferogram is typically multiplied by a suitable function before the transformation. This process, known as apodization, involves multiplying the interferogram by a function prior to the Fourier transformation to remove false sidelobes introduced due to the finite limits of optical path displacement [41].

4.1.2 Infrared spectroscopic ellipsometry

Spectroscopic ellipsometry is a non-contact non-destructive experimental method that serves primarily the purpose of characterizing thin films by determining their thickness, and optical constants (complex refractive index). However, it can be also applied to analysis of composition, crystallinity, roughness, doping concentration and other material properties associated with a change in optical response while providing sensitivity necessary to measure nanometer-scale layers used in microelectronics [42].

Principles of ellipsometry

Ellipsometry is based on the analysis of the change in the polarization state of light when reflected from or transmitted through a material structure. Generally, ellipsometric studies are carried out mostly in the reflection mode that is not restricted by the transparency of the ambient-film-substrate system for accessibility of the transmitted light [43]. The measurements conducted in this thesis were also performed solely within the reflection regime, so the principle of the method will be explained using this particular geometry.

Polarization is an intrinsic property of any transverse wave. Light represented by electromagnetic waves shares this property. For the description of light polarization, it is adequate to discuss the behaviour of the electric field component in time and space. The electric field is always orthogonal to the propagation direction. Hence, a wave traveling along the z-direction can be described by its x- and y- components. When the electric field vectors are randomly oriented in all directions perpendicular to the propagation direction, the light is considered unpolarized. If the electric field vectors follow a specific pattern in space, the light is considered polarized.

From the solution of Maxwell equations in a homogeneous isotropic medium in the

form of a plane wave, the components of the electric field $\vec{E}$ are

$$E_x = E_{x0} \sin(kz - \omega t + \varphi_x), \tag{4.5}$$

$$E_y = E_{y0} \sin(kz - \omega t + \varphi_y), \tag{4.6}$$

where ω is the circular frequency, φ_x and φ_y are constants and k is the wavenumber related to the wavelength of the incident radiation as

$$k = \frac{2\pi}{\lambda}. \tag{4.7}$$

From Eq. 4.5 and Eq. 4.6 it is possible to derive equation of ellipse:

$$\left(\frac{E_x}{E_{x0}}\right)^2 - 2\frac{E_x}{E_{x0}}\frac{E_y}{E_{y0}}\cos\Delta + \left(\frac{E_y}{E_{y0}}\right)^2 = \sin^2\Delta, \tag{4.8}$$

where Δ is the phase shift between the x- and y-components of the electric field defined as

$$\Delta = \varphi_y - \varphi_x. \tag{4.9}$$

There are three distinguishable polarization types, schematically depicted in Fig. 4.2. Eq. 4.8 describes the general elliptical polarization state of light when the phase shift and the amplitudes E_{x0} and E_{y0} have arbitrary values. If $E_{x0} = E_{y0}$ and $\Delta = \pm\pi/2$, Eq. 4.8 is reduced to equation of a circle and the light is described as circularly polarized. If Δ is equal to an integer multiple of π and Eq. 4.8 is reduced to equation of a line and the light is described as linearly polarized. The relative amplitudes E_{x0} and E_{y0} determine the resulting orientation.

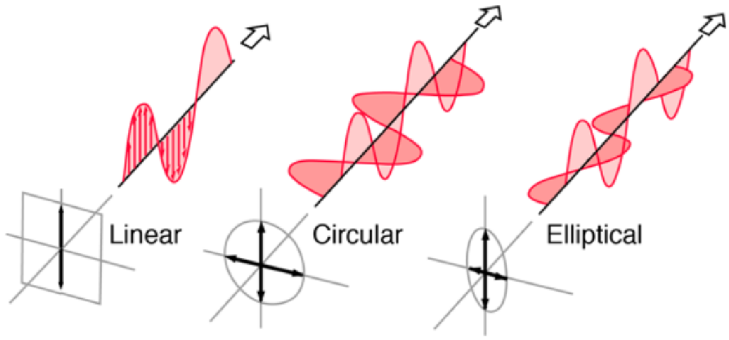

Figure 4.2: Linear, circular and elliptical polarization and projection of the electric field x- and y-components onto a plane perpendicular to the propagation direction [44].

Upon reflection at a surface in the ellipsometry measurements, linearly polarized radiation generally becomes elliptically polarized. The polarization change is represented by two values extracted from the measurements, the phase difference, Δ, and the angle

Ψ defined as

$$\tan \Psi = \frac{E_{x0}}{E_{y0}}. \tag{4.10}$$

The two ellipsometric parameters can be combined into a single parameter, ρ, which relates to the complex Fresnel reflection coefficients r_p and r_s through the following equation:

$$\rho = \tan \Psi e^{i\Delta} = \frac{r_p}{r_s}. \tag{4.11}$$

When considering reflection from a surface, the polarization of light is conventionally described in terms of two components: p-polarized and s-polarized light. P-polarized light has its electric field in the plane of incidence, while s-polarized light has its electric field perpendicular to this plane. The plane of incidence is defined as the plane that contains both the incident light ray and the normal to the surface at the point of incidence (see Fig. 4.3).

The complex Fresnel reflection coefficents for s- and p-polarization are derived from the boundary conditions of the interface for the tangential components of $\vec{E}$ and Snell's laws as

$$r_s = \frac{E_{rs}}{E_{is}} = \frac{N_1 \cos(\theta_i) - N_2 \cos(\theta_t)}{N_1 \cos(\theta_i) + N_2 \cos(\theta_t)}, \tag{4.12}$$

$$r_p = \frac{E_{rp}}{E_{ip}} = \frac{N_1 \cos(\theta_t) - N_2 \cos(\theta_i)}{N_1 \cos(\theta_t) + N_2 \cos(\theta_i)}. \tag{4.13}$$

In these equations, θ_i and θ_t denote the angles between the normal to the interface and the incident and transmitted beams, respectively. The terms N_1 and N_2 are the complex refractive indices of the materials forming the interface, N_1 represents the medium of the incident light (the surrounding medium), while N_2 represents the medium into which the light is transmitted.

The complex refractive index, defined as

$$N(\omega) = n(\omega) + ik(\omega), \tag{4.14}$$

where ω is the angular frequency of the light interacting with the material, encapsulates the spectral dependency of the material's optical properties. The real part, $n(\omega)$, describes the phase velocity of light in the material, while the imaginary part, $k(\omega)$, represents the material's absorption of the light. Understanding the refractive index is crucial for material characterization. Specifically, from ellipsometric data, we aim to determine the refractive index to assess the material's optical properties.

Direct calculation of the optical constants n and k from the measured ellipsometric parameters Δ and Ψ is only possible when studying the simplest possible system, which is a single optical interface. It is given by the following equation: [45]:

$$N_2 = N_1 \tan(\theta_i) \sqrt{1 - \frac{4\rho \sin^2(\theta_i)}{(\rho + 1)^2}}. \tag{4.15}$$

For more complex structures involving multiple interfaces (layers), the concept of the effective refractive index becomes essential. The effective refractive index, integrates the contributions from all layers in the structure, providing a comprehensive description of the optical response. A detailed description of calculations the complex Fresnel coefficients for the multilayer systems using the Jones matrix formalism and introducing also the thicknesses of the layers can be found for example in [46].

Furthemore, in the case of studying more complex systems, for example, if only a thin layer on a substrate is involved, n, k and the thickness of the layer at known values of the optical constants of the substrate cannot be obtained by direct calculation. In general, the procedure is as follows: a set of ellipsometric spectra is obtained experimentally for several different incidence angles. Then, a suitable model is utilized for the system under study and the aim is to fit this model to obtain model parameters so that the calculated data are as close as possible to the measured values. The accuracy of the model fit is evaluated by the mean squared error [45].

Experimental setup

Scheme of a typical configuration of optical components of an ellipsometer is shown in Fig. 4.3. The unpolarized light generated by the light source is first linearly polarized by the polarizer. This polarized light then passes through the first compensator, which is an optional component that introduces a known phase shift between the orthogonal components of the light. This phase shift is usually introduced for creating elliptically polarized light, which interacts more sensitively with the sample's surface.

Upon striking the sample at an oblique angle, the light reflects and its polarization state changes according to the sample's optical properties. The reflected light then passes through a second optional compensator, which helps to decode the changes imparted by the sample by introducing another controlled phase shift.

Next, the analyzer, another polarizing element, is used to investigate the reflected light. By rotating the analyzer and measuring the intensity of light that passes through

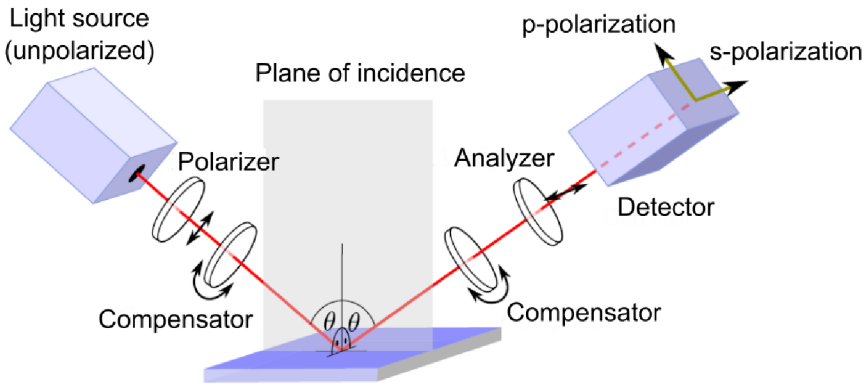

Figure 4.3: Schematic illustration of a conventional configuration of an ellipsometer. Adapted from [47].

it, we can determine the ellipsometric parameters, Δ and Ψ. Finally, the light reaches the detector, where the intensity measurements are recorded. The detector data, combined with the known input polarization state and the adjustments made by the compensators and analyzer, allows for the precise calculation of the sample's optical properties.

The instrument used for the measurements conducted in this work was J. A. Woollam IR-VASE Spectroscopic Ellipsometer. The spectroscopic scans in this instrument are done using an FTIR spectrometer as the light source.

4.1.3 Measurement results

The spectroscopic methods described above were employed to measure the losses and optical constants of the components of the interband cascade device structures. Measurements were conducted progressively, starting with the substrates, followed by the substrate with buffer layers, and finally the substrate with buffer layer, superlattice cladding, and active regions. All of the samples were grown and provided by the Optoelectronic Epitaxy group at TU Wien.

Substrate

The transmission of mid-infrared radiation in the wavenumber range from 6000 to 1000 cm^1 through different substrate samples was measured in the FTIR. The set of samples consisted of cleaved single side polished 500 μm thick wafers of different III-V semiconductors, InAs, p-doped GaSb and n-doped GaSb. The doping of the n-GaSb was $2 \cdot 10^{17}\text{cm}^{-3}$ and the doping of the p-GaSb was $5 \cdot 10^{16}\text{cm}^{-3}$. These three semiconductors were considered due to them being the most commonly used substrates for the interband cascade devices lattice-matched growth. The measured spectral intensity was divided by the reference spectra for the transmission through vacuum to obtain the transmittance $T(\tilde{\nu})$ of the individual samples. The combined transmittance spectra is shown in Fig. 4.4.

From the measured data, we can see that the transmittance is overall highest for p-GaSb and lowest for InAs. This confirmes the expected results. In p-GaSb, the dominant charge carriers are holes. These holes have a lower effective mass compared to electrons ... in n-GaSb, resulting in higher mobility and lower absorption coefficient for free carrier absorption (see Eq. 3.7). InAs has a narrower bandgap compared to GaSb, resulting in higher absorption of photons in the mid-infrared.

The bandgap energy can be also determined from the measured data by analyzing the onset of absorption abvove the bandgpap, corresponding to the transmittance abruptly dropping to zero. This sharp decrease in transmittance corresponds to the absorption edge, marking the energy threshold required to excite electrons across the bandgap. The estimation of the bandgap energy from these measurements is for InAs $E_{\text{g,InAs}} \approx 0.34\,\text{eV}$ and for GaSb $E_{\text{g,InAs}} \approx 0.69\,\text{eV}$ at room temperature.

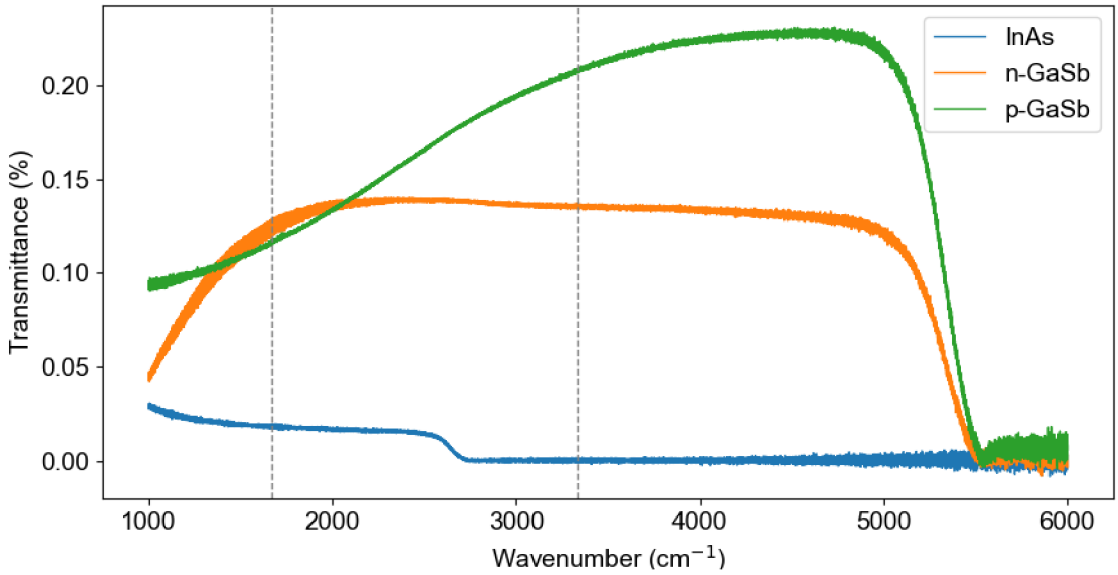

Figure 4.4: Transmittance spectra in dependency on the incident light wavenumber for InAs, p-GaSb, and n-GaSb 500 μm thick substrates.The vertical lines indicate the wavelength region 3–6 μm where the interband cascade devices operate.

The wavelength range in which interband cascade devices operate is marked in the plot by dashed vertical lines. From these measurements, we can conclude that out of these substrate materials, the one that would be most suitable for substrate-emitting ICLEDs is p-GaSb due to the fact that the light transmitting through this material is the least attenuated.

The optical constanst n and k of the p-GaSb substrate were also measured in the ellipsometry setup and subsequently fitted. The fit of the optical constants for this particular substrate and the doping was saved in the material library and can be utilized in future measurements as reference data for measurements of structures based on this substrate.

Buffer on GaSb substrate

Next, several samples with different thickness of n-GaSb buffer layers on top of the previously measured p-GaSb substrate were measured in the ellipsometry setup. The overview of the measured samples and their growth parameters is in Tab. 4.1.

The measured data were fitted by the general Drude model. The Drude model allowed us to enter the material type, doping levels and carrier mobility of the materials of the substrate and the buffer layers. However, when fitting the thickness of the layers, the model converged to zero. One of the hypothesis to explain the fact that the model didn't converge to the real values was based on the possibility that the charge carriers from the substrate could have flooded the thin buffer layer. This possibility was outruled by calculation of the charge carrier density across the PN junction created by the p- and n-doped GaSb. The calculation was done considering the depletion

Table 4.1: Parameters of the different measured GaSb buffer layers. p_{Ga} and p_{Sb} are the partial pressures of Ga and Db in the MBE chamber. The valve position given in mil (thousandths of an inch) controls the flux of Sb atoms (higher value means higher flux). RMS is the root mean square rougness of the sample surface. The growth temperature was $T_{\mathrm{growth}} = 485\,^{\circ}\mathrm{C}$.

t (nm)	p_{Ga} (Torr)	p_{Sb} (Torr)	Sb valve position (mil)	RMS (nm)
70	$3.615 \cdot 10^{-7}$	$1.228 \cdot 10^{-6}$	100	1.899
70	$3.744 \cdot 10^{-7}$	$1.696 \cdot 10^{-6}$	120	0.377
100	$3.767 \cdot 10^{-7}$	$1.434 \cdot 10^{-6}$	110	0.990
100	$3.717 \cdot 10^{-7}$	$1.704 \cdot 10^{-6}$	120	0.808
300	$3.609 \cdot 10^{-7}$	$1.438 \cdot 10^{-6}$	110	0.462
300	$3.903 \cdot 10^{-7}$	$1.700 \cdot 10^{-6}$	120	0.236

approximation [48]. The results based on this approximation are plotted in Fig 4.5. The charge carrier density is plotted over position, while the substrate-buffer interface is set to zero, the vertical lines in the plot indicate the buffer-air interface. We can see that in comparison to the thickness of the buffer layer, the depletion region impacts only very small part of the layer. Precisely, the the width of the depletion region on the n-type side of the junction was approximated as $x_{\mathrm{n}} = 3.7\,\mathrm{nm}$. The width of the whole depletion region was $w = 150.2\,\mathrm{nm}$.

Another possibility is that the surface (buffer-air) effects the results. In the case of the buffer layers, especially when they are relatively thin, the surface properties might become crucial. If there are surface states or defects at the buffer-air interface, they can affect the carrier dynamics and the optical properties of the material. This could lead to deviations from the ideal behavior assumed by the Drude model, making it difficult to fit the thickness accurately. Additionally, the presence of any surface roughness can also complicate the fitting process. Surface roughness can scatter light, altering the effective optical properties observed by ellipsometry and making it challenging to accurately determine the thickness of the buffer layer. To include the surface effects into the fitting would require further and more complicated models. To include the surface effects into the fitting would require further and more complicated models, which are beyond the scope of this thesis.

However, from the raw data, it was possible to see that the imaginary part of the refractive index indicated higher losses in certain parts of the spectra for the 70nm buffer sample with the highest surface roughness of RMS = 1.899 nm.

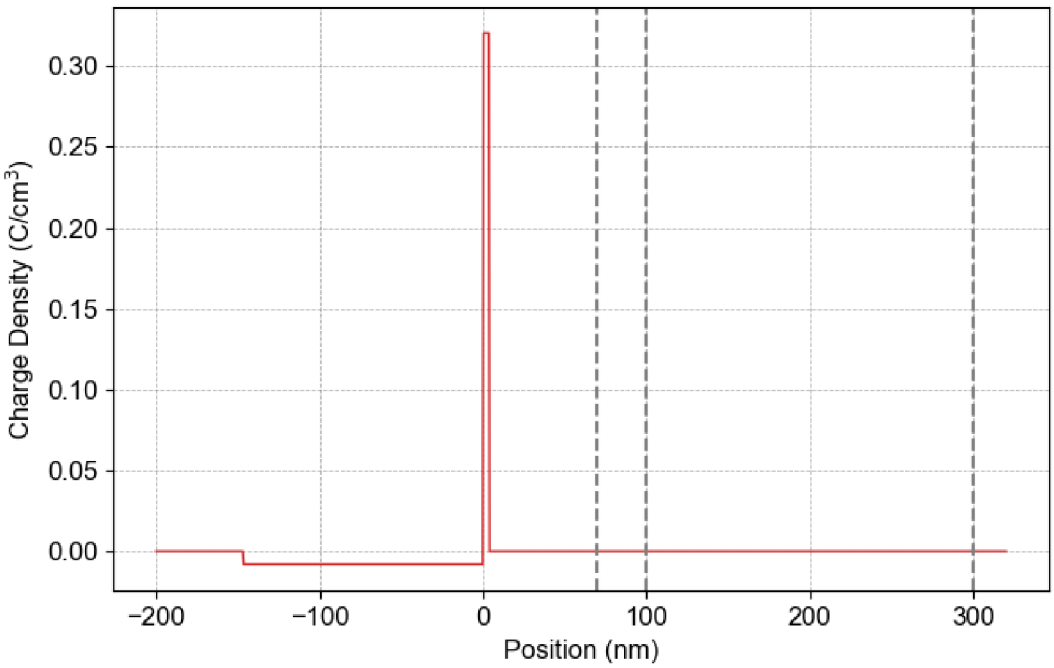

Figure 4.5: Approximation of charge density dependent on the position across the depletion region. Zero in the position coordinate marks the interface between n-doped GaSb substrate (negative values) and p-doped GaSb buffer (positive values). The vertical lines mark the position of the buffer-air interfaces for buffers of different thicknesses.

ICL waveguide structure

Lastly, two samples (ICL1 and ICL2) consisting of the whole ICL structure for emission at $\lambda = 4.3\,\mu$m provided by nanoplus were measured. The ellipsometry data for the incidence angle 60° comparing the optical constant k for these two samples are plotted in Fig.4.6. The sample ICL1 was slightly lower doped.

The comparison between the optical constant k for the sample ICL1 and the absorbance extracted from FTIR measurement of the same sample are shown in Fig. 4.7.

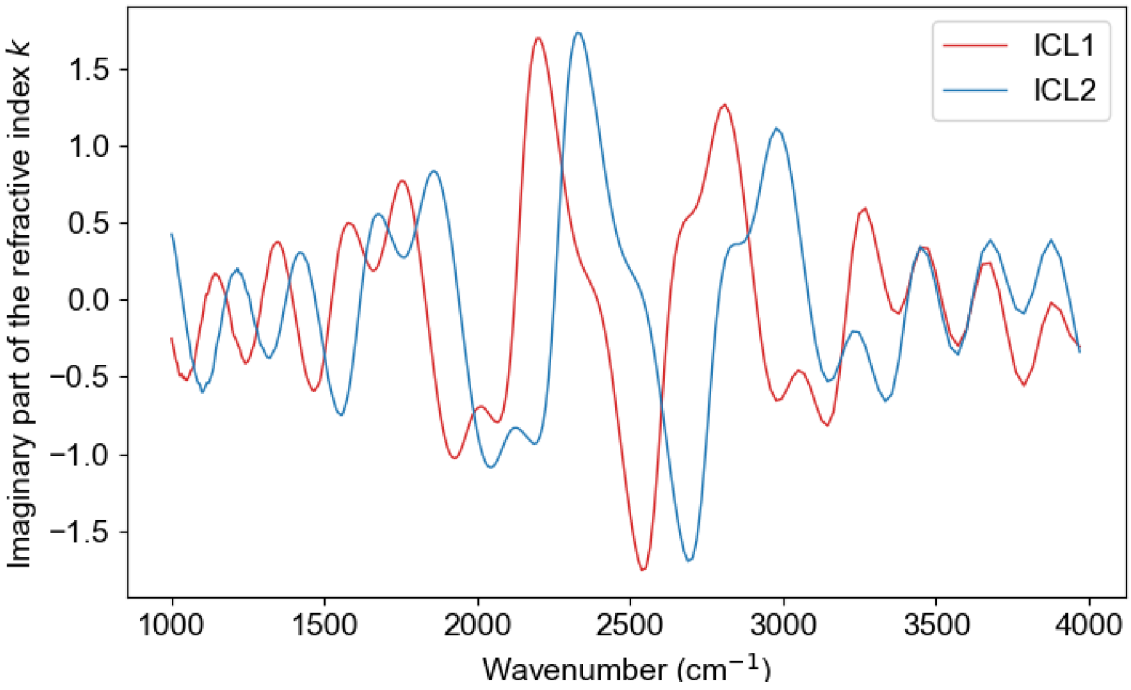

Figure 4.6: Comparison of data obtained from ellipsometric measurement for the incidence angle 60° for the different ICL samples.

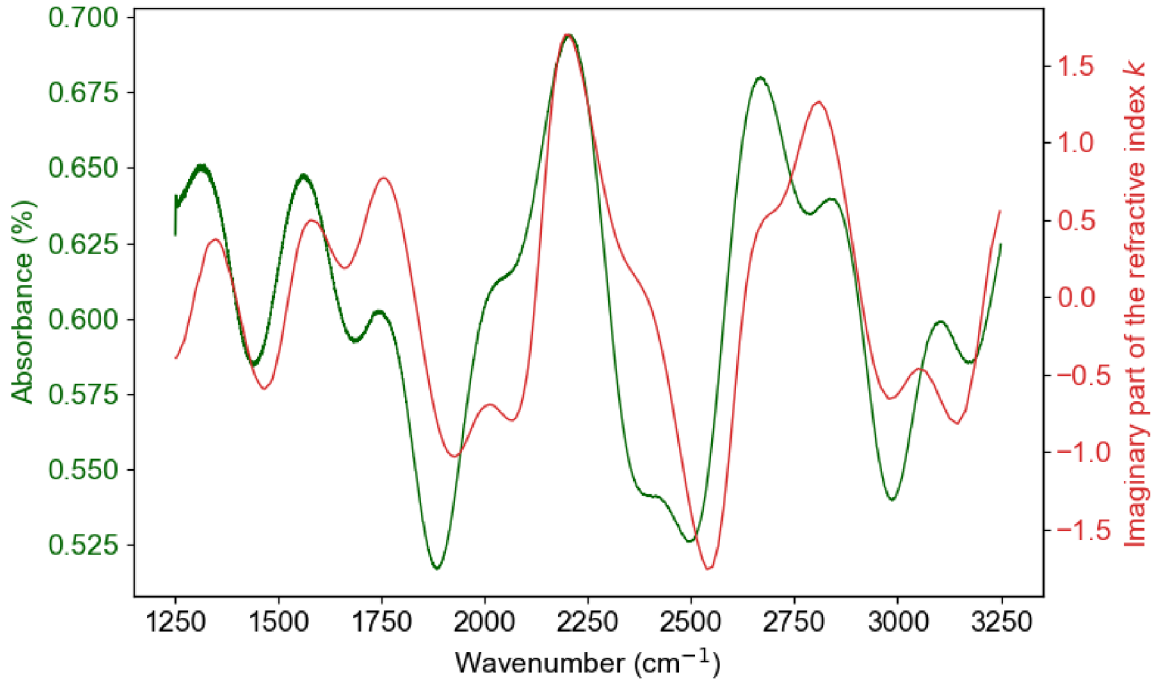

Figure 4.7: Comparison of the absorbance data from FTIR measurement and the imaginary part of the refractive index k from ellipsometry measurement plotted against the wavenumber for the sample ICL1.

4.2 ICL waveguide characterization

In order to characterize the voltage-dependency of the losses due to the valence intersubband absorption in the W quantum well influencing interband cascade devices' performance operating at wavelengths $> 4\mu$m, custom optical setup for waveguide characterization was constructed. To fit the data measured using an ICL as a waveguide and subsequently extract the ICL losses, a model based on the transfer matrix method was utilized.

4.2.1 Waveguide loss characterization

Fabry-Perot method

The main principle of loss characterization in this setup is based on measuring changes in the optical power transmitted through a waveguiding structure. One of the main challenges in characterizing optical waveguides is accurately measuring propagation losses. Several approaches in the literature provide precise results, but the Fabry-Perot interferometer method exhibits the least uncertainties. It is particularly well-suited for characterizing waveguide losses even below 1 dB/cm [49].

The Fabry-Perot interferometer method relies on measuring the contrast of a Fabry-Perot cavity. Structures composed of III-V semiconductors have a large effective refractive index, resulting in a significant refractive index mismatch and high internal reflectivity at the waveguide-air interfaces. Consequently, the waveguide forms a Fabry-Perot resonator. Multiple reflections from the waveguide facets interfere, creating fringes in the transmitted signal. By analyzing the amplitude and periodicity of this periodic modulation, which occurs when the optical path length of the waveguide changes, we can determine the propagation loss and the effective refractive index of the waveguide. Changes in the optical path can be induced by altering the waveguide's temperature, as the optical path length depends on the physical length of the waveguide and its refractive index, both of which are temperature-dependent. Alternatively, the optical path can be changed by tuning the probe laser wavelength [50].

In 2004, Revin et al. [51] used the Fabry-Perot technique to measure losses in mid-infrared semiconductor laser waveguiding structures with a probe laser wavelength different from the emission wavelength of the laser under investigation. A similar approach was chosen to determine the attenuation of light in the ICL waveguides.

Optical setup

The schematic illustration of the waveguide characterization setup built in an optical laboratory at the Institute of Solid State Electronics at TU Wien are depicted in Fig. 4.8. It consist of several optical components and a signal detection system.

As the probing laser, a distributed-feedback (DFB) ICL (nanoplus) emitting single-mode cw radiation at $\lambda \approx 4.6\,\mu$m was utilized. The sealed housing system of the laser

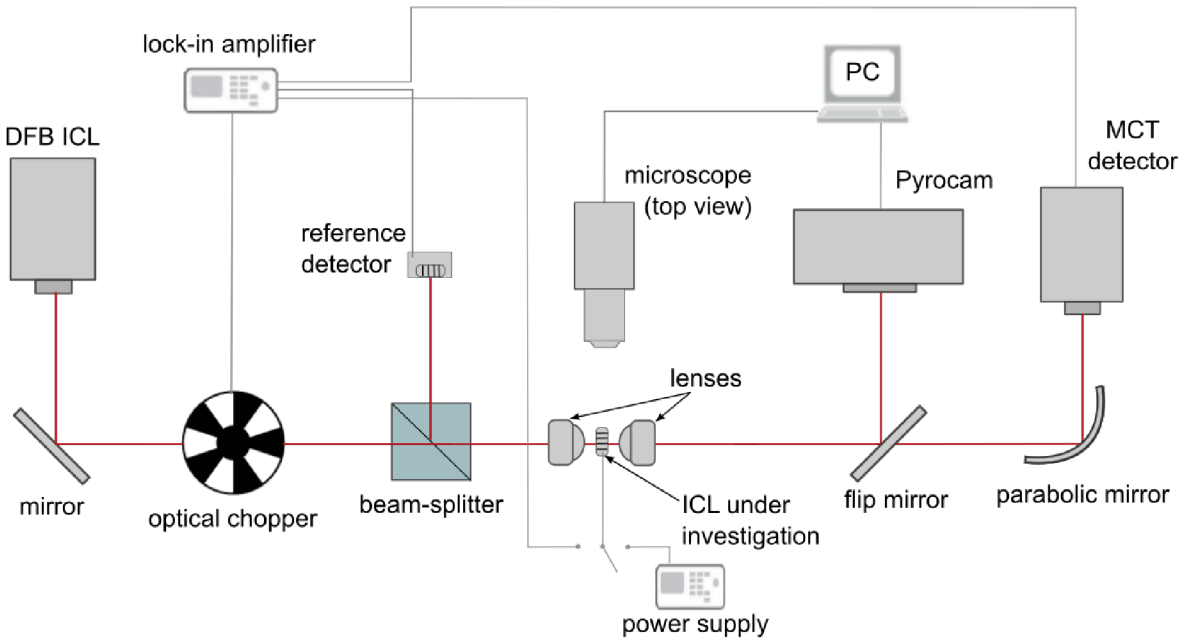

Figure 4.8: a) Schematic illustration of the experimental setup for waveguide characterization measurements.

incorporated a built-in lens, providing collimated beam, and thermoelectric cooling and heating in combination with Peltier elements for temperature control and for ensuring the stability of the emission. QubeCL driver was used to optimize and control the laser's operation parameters. The laser is exchangeable if different emission wavelength is needed for different applications.

The laser beam, modulated by a mechanical optical chopper for better signal acquisition, travels through free space to the lenses-waveguide system, which is the most important part of the setup. For end-fire in-coupling, which is a way to excite guided modes by spatial mode matching by precisely focusing light onto the facet of the waveguide, and for out-coupling, lenses with high numerical aperture are used. Light coupling into and out of the waveguide under investigation was achieved using an optical system consisting of two aspheric lenses (Thorlabs, NA = 0.85), which focused and collimated the free-space mode, respectively. The lenses in holders were placed on manual 3-axis (xyz) translation stages to adjust the alignment with respect to the beam. The lens holders also allowed tilt adjustment. The waveguide samples were mounted on a holder attached to another translation stage used to move the waveguide with respect to the lenses.

The most crucial part of the measurement effecting the precision is the alignment of the waveguiding structure with the lenses. It is also the most challenging due to operation in the mid-infrared spectral region, where the beam can be visualized only using thermal paper, and also due to the relatively small dimensions of the waveguide facet resulting in sensitivity to the alignment in range of tens of nm.

Therefore, the alignment of the setup was done in the following way. First, the lenses were aligned to the probing laser beam in respect to the Pyrocam IV (Ophir), a pyroelectic array camera allowing the modal analysis of the incident beam. When the lenses are properly aligned, the displayed beam has a Gaussian shape. The flip mirror then allows us to direct the beam to thermoelectrically cooled mercury cadmium telluride (MCT) detector with an integrated pre-amplifier (Vigo) connected to a digital lock-in amplifier (Zurich instruments). The tilt of parabolic mirror focusing the beam onto the detector was adjusted to maximize the signal.

After the alignment of the lenses, the outcoupling lens was brought back and the measured sample was inserted between the lenses. The measured samples consisting of several parallel ICLs were mounted on a copper holder shown in Fig 4.9. The sample was using solder paste to the narrow part of the holder. The ICLs were wire-bonded to the PCB (printed circuit board) glued to the broader part of the holder. To align the ICL with the first lens, it was used as a photodetector. To measure the photocurrent generated in the ICL structure by coupling in the focused beam, the PCB was connected to the lock-in amplifier. By moving the ICL, the highest possible signal retrieved by the lock-in amplifier can eventually be found. Consequently, this allows us to also determine the position of the focal spot of the in-coupling lens. That is because reaching the signal maximum means that the beam is perfectly centered and focused on the front facet of the ICL ridge. Afterwards, the outcoupling lens was brought back to the position indicated by the maximum signal of the outcoupled light detected by the MCT.

For the purpose of alignment with regular waveguides that cannot be used as pho-

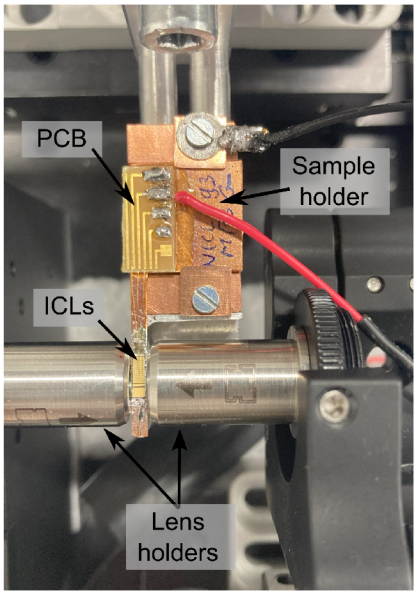

Figure 4.9: Picture of the sample holder with the ICL waveguide sample mounted on the narrow part of the holder inserted betwwen the lasers. The ICLs are wire-bonded to the PCB on the broader part of the holder. The PCB is electrically connected either to the lock-in amplifier or the power supply.

todetectors, the waveguide and the second lens can be briefly substituted with and interband cascade photodetector mounted on a PCB attached to another stage. The position of the photodetector can be monitored with the help of a homemade microscope constructed using Thorlabs cage system and consisting of a 50x objective (ZEISS, NA = 0.42, infinity-corrected), a lens, light illumination syste,, and a CMOS camera (Blackfly USB3, Teledyne FLIR). After finding the focal spot with the photodetector, the pixel coordinates of the photodetector's front facet would be saved and subsequently the waveguide placed so that the front facet of the waveguide is aligned to the same spot. For our purposes the imaging system was used only for observing the ICL during measurements for monitoting the ICL's position.

To measure the signal attenuation dependency on operating current/voltage, the ICL under investigation was connected to a dual-channel DC power supply (Keithley Instruments) during the measurements. The sample was connected to the power supply in the same manner as during the alignment process to the lock-in amplifier.

4.2.2 Transfer matrix method

To fit the data acquired from the measurements, we used a numerical model for the transmission through a Fabry-Perot cavity, which was obtained using the transfer matrix method. The transfer matrix method is a method used mostly in optics to analyze the propagation of electromagnetic waves through a multi-layered medium. It can be exploited to simulate and aid the design of real optical components such as lenses, Bragg mirrors, antireflection coatings, waveplates, or polarization converters [52].

The transfer matrix describes the transformation of electromagnetic field when it passes through one material layer. For light with given wavelength λ propagating through the layer at normal incidence the transfer matrix is defined as

$$M = \begin{pmatrix} \cos k_0 N d & i\frac{Z_0}{N} \sin k_0 N d \\ i\frac{N}{Z_0} \sin k_0 N d & \cos k_0 N d \end{pmatrix}, \tag{4.16}$$

where d is the thickness of the layer, $N(\lambda)$ is the complex refractive index of the material used for this layer, Z_0 is a constant defined as $Z_0 = \mu_0/\epsilon_0$, and k_0 the magnitude of the wave vector defined as $k_0 = 2\pi/\lambda$.

The change in the electromagnetic field components, the electric field E and the magnetic field H, over the distance d for propagation along x is then calculated using the transfer matrix as

$$\begin{pmatrix} E(x+d) \\ H(x+d) \end{pmatrix} = M \cdot \begin{pmatrix} E(x) \\ H(x) \end{pmatrix}. \tag{4.17}$$

The amplitude reflectance and transmittance coefficients of the light upon incidence with an interface were defined as

$$r = \frac{N_0 Z_0 \mathrm{M}_{00} + N_0 N_s \mathrm{M}_{01} - {Z_0}^2 \mathrm{M}_{10} - N_s Z_0 \mathrm{M}_{11}}{N_0 Z_0 \mathrm{M}_{00} + N_0 N_s \mathrm{M}_{01} + Z_0^2 \mathrm{M}_{10} + N_s Z_0 \mathrm{M}_{11}}, \tag{4.18}$$

$$t = \frac{2 \cdot N_0 \cdot Z_0}{N_0 \cdot Z_0 \cdot \mathrm{M}_{00} + N_0 \cdot N_s \cdot \mathrm{M}_{01} + Z_0^2 \cdot \mathrm{M}_{10} + N_s \cdot Z_0 \cdot \mathrm{M}_{11}}, \tag{4.19}$$

where N_0 is the refractive index of the medium that the light is traveling through and N_s is the refractive index of the medium into which part of the light is transmitted. The reflectance and transmittance determining the fraction of the incident intensity transmitted and reflected by the interface are given by

$$R = |r|^2 \tag{4.20}$$

$$T = \frac{N_s}{N_0} \cdot |t|^2 \tag{4.21}$$

.

For multilayer system consisting of N layers, the matrix characterizing the whole system M_{total} is obtained by sequentially multiplying the transfer matrices M_i for each of the layers:

$$M_{\text{total}} = M_N \cdot M_{N-1} \cdot \ldots \cdot M_2 \cdot M_1. \tag{4.22}$$

The coeffiecients r and t of the entire system can then be derived from the elements of M_{total} using the same formulas as before.

4.2.3 Experiment and results

The ICL under investigation (Fig. 4.10) measured in the waveguide characterization setup to prove the dependency of the valence intersubband absorption on bias had emission wavelength of 3.3 μm and the thickness of the hole quantum well in the active quantum well system in the ICL structure was 3 nm.

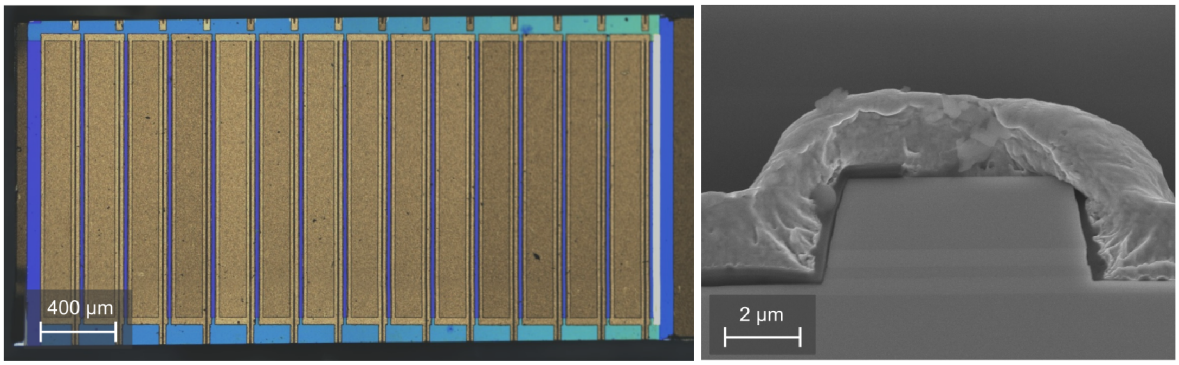

Figure 4.10: Optical microscope picture of the measured sample with several parallel ICL wavegudis (left) and SEM picture of the ICL's facet.

The probing laser with wavelength 4.6 μm was chosen to specifically target the valence intersubband transitions while also avoiding resonant absorption between the laser optical transition states. To measure the transmission losses using the Fabry-Perot method, the probing laser wavelength was tuned by changing the operating current in the range 4.604–4.610 μm.

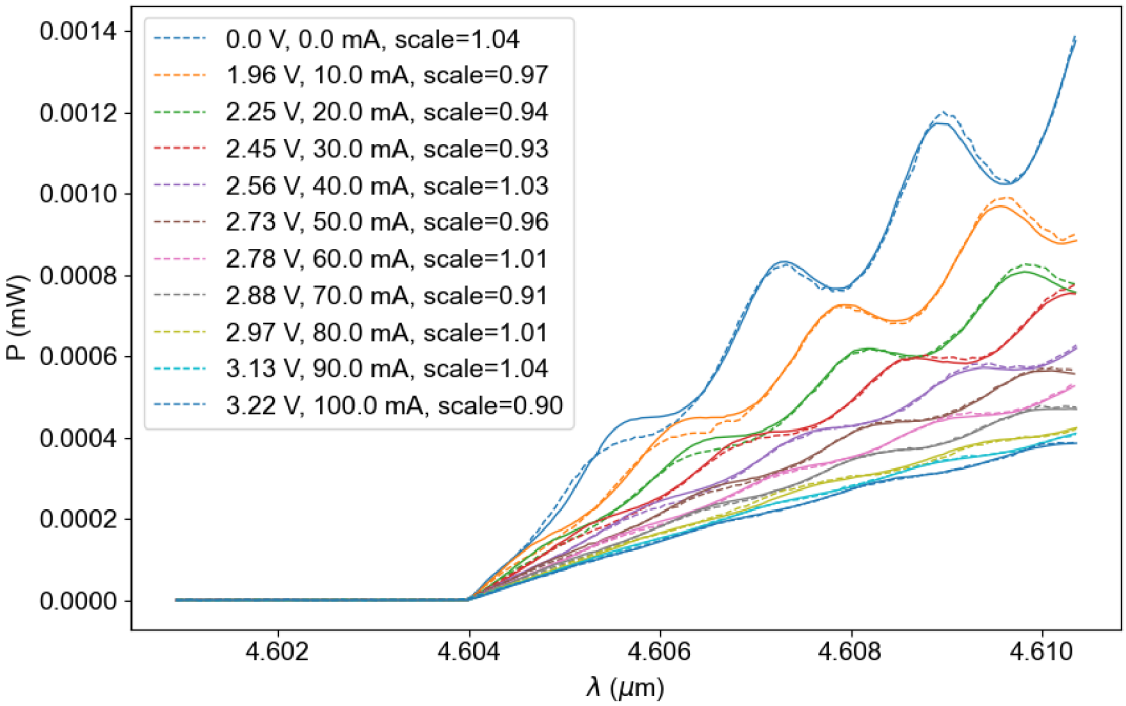

Figure 4.11: The measured and fitted data of the transmitted power in dependence on the wavelength.

The measured and fit data are shown in Fig. 4.11. We can see already from this plot that with higher current/voltage, the power of the transmitted light and the amplitude of the fringes are decreasing.

Transmission losses obtained from the model utilizing the transfer matrix method in dependancy on the operating current and voltage are shown in Fig 4.12.

Extracted waveguide losses determined from the measueremnt under different operating current and bias confirm the pivotal role of the valence intersubband absorption as when higher current introduces more carriers (holes) into the ICL structure, the probability of the intersubband transition rises together with the losses.

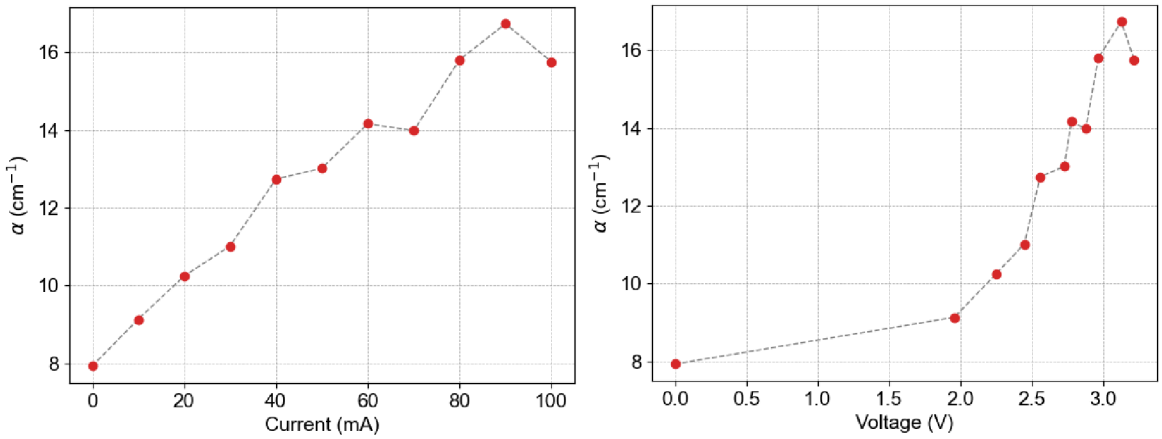

Figure 4.12: Losses extracted from the fitting plotted against current and voltage applied to the ICL waveguide under investigation.

5. Conclusion

This thesis presents a study on the material characterization methods and modeling of interband cascade devices, focusing especially on interband cascade light emitting devices (ICLEDs). By investigating the optical properties of interband cascade structures, the aim was to verify possible use of the presented methods on the way to the devices' optimization, which could lead to enhancement of their efficiency and applicability in mid-infrared photonic integrated circuits in sensing and on-chip spectroscopy.

After introduction of the interband cascade devices and the loss mechanisms present in these devices causing degradation of their performance, the focus was placed on various experimental methods, specifically spectroscopic ellipsometry, Fourier transform infrared spectroscopy (FTIR), and waveguide loss characterization method. These methods were employed to extract critical material parameters, providing a deeper understanding of the optical properties of the interband-cascade structures.

The ellipsometry and FTIR measurements focused on extraction of optical parameters and transmittance of different structural components of the interband cascade devices that could be useful in choosing the suitable materials for the fabrication of ICLEDs.

Among the different loss mechanisms, particular attention was given to valence intersubband absorption, which significantly degrades the performance of interband cascade devices in the mid-infrared wavelength region above 4 μm. Experimental characterization of ICL waveguides revealed the impact of this absorption under various operating conditions, providing valuable insights for further device optimization.

The existing transport model was extended to incorporate the spontaneous emission, which is the dominant emission mechanism in ICLEDs. This extension allowed for more accurate predictions of ICLED performance, particularly in terms of efficiency and emission characteristics.

Future work could explore further refinements of the transport model and the development of new ICLED structures with enhanced performance. Additionally, integrating these devices into photonic integrated circuits remains a promising avenue for creating compact, efficient, and versatile mid-infrared sensing systems.

Bibliography

[1] Hall, R. N.; Fenner, G. E.; Kingsley, J. D.; et al.: Coherent Light Emission From GaAs Junctions. *Phys. Rev. Lett.*, vol. 9, 1962: p. 366–368, doi:10.1103/PhysRevLett.9.366.

[2] Popa, D.; Udrea, F.: Towards Integrated Mid-Infrared Gas Sensors. *Sensors*, vol. 19, 9, 2019, doi:10.3390/s19092076.

[3] Yang, R. Q.; Li, L.; Huang, W.; et al.: InAs-Based Interband Cascade Lasers. *IEEE Journal of Selected Topics in Quantum Electronics*, vol. 25, 6, 2019: p. 1–8, doi:10.1109/JSTQE.2019.2916923.

[4] O'Hanlon, J.: *A User's Guide to Vacuum Technology*. Hoboken: Wiley-Interscience, 3. ed., 2003, ISBN 9780471467168.

[5] Lüth, H.: *Solid Surfaces, Interfaces and Thin Films*. Springer Cham, 6 ed., 2014.

[6] Cho, A.: Growth of III–V semiconductors by molecular beam epitaxy and their properties. *Thin Solid Films*, vol. 100, 4, 1983: p. 291–317, doi:10.1016/0040-6090(83)90154-2.

[7] Downs, C.; Vandervelde, T.: Progress in Infrared Photodetectors Since 2000. *Sensors*, vol. 13, 04, 2013: p. 5054–5098, doi:10.3390/s130405054.

[8] Yang, R. Q.: Band alignment of and lattice constant of materials used in interband cascade laser. 2014, Wikimedia Commons, [Online]. URL `<https://commons.wikimedia.org/w/index.php?curid=32561802>`

[9] Yang, R. Q.: Interband cascade (IC) lasers. In *Semiconductor Lasers*, Woodhead Publishing, 2013, ISBN 9780857091215, p. 487–513, doi:10.1533/9780857096401.3.487.

[10] Yang, R. Q.: Infrared laser based on intersubband transitions in quantum wells. *Superlattices and Microstructures*, vol. 306, 1995: p. 77–83, doi:10.1006/spmi.1995.1017.

[11] Faist, J.; Capasso, F.; Sivco, D. L.; et al.: Quantum Cascade Laser. *Science*, vol. 264, 5158, 1994: p. 553–556, doi:10.1126/science.264.5158.553.

[12] Vurgaftman, I.; Bewley, W. W.; Canedy, C. L.; et al.: Rebalancing of internally generated carriers for mid-infrared interband cascade lasers with very low power consumption. *Nature Communications*, vol. 585, 2011.

[13] Meyer, J. R.; Hoffman, C. A.; Bartoli, F. J.; et al.: Type-II quantum-well lasers for the mid-wavelength infrared. *Applied Physics Letters*, vol. 67, 6, 1995: p. 757–759, doi:10.1063/1.115216.

[14] Meyer, J. R.; Bewley, W. W.; Canedy, C. L.; et al.: The Interband Cascade Laser. *Photonics*, vol. 7, 75, 2020, doi:10.3390/photonics7030075.

[15] Vurgaftman, I.; Meyer, J. R.; Ram-Mohan, L. R.: Band parameters for III–V compound semiconductors and their alloys. *Journal of Applied Physics*, vol. 89, 11, 2001: p. 5815–5875, doi:10.1063/1.1368156.

[16] Kim, M.; Canedy, C. L.; Bewley, W. W.; et al.: Interband cascade laser emitting at $\lambda = 3.75\mu$m in continuous wave above room temperature. *Applied Physics Letters*, vol. 92, 19, 2008: p. 191110, doi:10.1063/1.2930685.

[17] Vurgaftman, I.; Weih, R.; Kamp, M.; et al.: Interband cascade lasers. *Journal of Physics D: Applied Physics*, vol. 48, 03 2015: p. 123001, doi:10.1088/0022-3727/48/12/123001.

[18] Krier, A.; Repiso, E.; Al-Saymari, F.; et al.: Mid-infrared light-emitting diodes. In *Mid-infrared Optoelectronics*, Woodhead Publishing, 2020, ISBN 978-0-08-102709-7, p. 59–90, doi:10.1016/B978-0-08-102709-7.00002-4.

[19] Yang, R. Q.; Lin, C.-H.; Murry, S. J.; et al.: Interband cascade light emitting diodes in the 5–8 m spectrum region. *Applied Physics Letters*, vol. 70, 15, 1997: p. 2013–2015, doi:10.1063/1.118806.

[20] Das, N. C.: Increase in midwave infrared light emitting diode light output due to substrate thinning and texturing. *Applied Physics Letters*, vol. 90, 1, 2007: p. 011111, doi:10.1063/1.2430484.

[21] Das, N. C.: Nano-plasmon enhancement effect on MWIR light emitting diode performance. *Infrared Physics Technology*, vol. 55, 1, 2012: p. 166–169, doi:10.1016/j.infrared.2011.11.005.

[22] Kim, C. S.; Bewley, W.; Merritt, C.; et al.: Improved mid-infrared interband cascade light-emitting devices. *Optical Engineering*, vol. 57, 2018, doi:10.1117/1.OE.57.1.011002.

[23] Schäfer, N.; Scheuermann, J.; Weih, R.; et al.: High efficiency mid-infrared interband cascade LEDs grown on low absorbing substrates emitting >5 mW of output power. *Optical Engineering*, vol. 58, 2019, doi:10.1117/1.OE.58.11.117106.

[24] Díaz-Thomas, D. A.; Stepanenko, O.; Bahriz, M.; et al.: 3.3 µm interband-cascade resonant-cavity light-emitting diode with narrow spectral emission linewidth. *Semiconductor Science and Technology*, vol. 35, 12, 2020: p. 125029, doi:10.1088/1361-6641/abbebc.

[25] Canedy, C. L.; Bewley, W. W.; Tomasulo, S.; et al.: Mid-infrared interband cascade light emitting devices grown on off-axis silicon substrates. *Opt. Express*, vol. 29, 22, 2021: p. 35426–35441, doi:10.1364/OE.435825.

[26] Li, N.; Tao, L.; Yi, H.; et al.: Methane detection using an interband-cascade LED coupled to a hollow-core fiber. *Opt. Express*, vol. 29, 5, 2021: p. 7221–7231, doi:10.1364/OE.415724.

[27] Li, N. P.; Tao, L.; McSpiritt, J.; et al.: Room temperature detection of N2O using a resonant cavity mid-IR detector and interband cascade LED. *Optical Sensors and Sensing Congress 2022 (AIS, LACSEA, Sensors, ES)*, 2022, doi:10.1364/LACSEA.2022.LM3B.2.

[28] O'Reilly, E. P.; Jones, G.; Silver, M.; et al.: Determination of Gain and Loss Mechanisms in Semiconductor Lasers Using Pressure Techniques. *physica status solidi (b)*, vol. 198, 1, 1996: p. 363–373, doi:10.1002/pssb.2221980148.

[29] Sze, S. M.; Lee, M. K.: *Semiconductor Devices: Physics and Technology*. John Wiley & Sons, 3. ed., 2012, ISBN 9780470537947.

[30] Shockley, W.; Read, W. T.: Statistics of the Recombinations of Holes and Electrons. *Physical Review*, vol. 87, 1952: p. 835–842, doi:10.1103/PhysRev.87.835.

[31] Satpathy, R.; Pamuru, V.: Making of crystalline silicon solar cells. In *Solar PV Power*, Academic Press, 2021, ISBN 978-0-12-817626-9, p. 71–134, doi:10.1016/B978-0-12-817626-9.00004-6.

[32] Goetzberger, A.; Knobloch, J.; Voß, B.: *Crystalline Silicon Solar Cells*. John Wiley & Sons, 1998, doi:10.1002/9781119033769.ch1.

[33] Fu, H.; Zhao, Y.: Efficiency droop in GaInN/GaN LEDs. In *Nitride Semiconductor Light-Emitting Diodes (LEDs)*, Woodhead Publishing, 2. ed., 2018, ISBN 978-0-08-101942-9, p. 299–325, doi:10.1016/B978-0-08-101942-9.00009-5.

[34] Li, S.: *Semiconductor Physical Electronics*. Springer, 2. ed., 2007.

[35] Knötig, H.: *Interband cascade lasers and detectors: From active region design to devices*. PhD Thesis, 2022. TU Wien, Austria.

[36] Chandola, A.; Pino, R.; Dutta, P. S.: Below bandgap optical absorption in tellurium-doped GaSb. *Semiconductor Science and Technology*, vol. 20, 8, 2005: p. 886, doi:10.1088/0268-1242/20/8/046.

[37] *Silicon Photonics: Fundamentals and Devices*. John Wiley Sons, Ltd, 2012, doi:10.1002/9781119945161.ch4.

[38] Childs, G. N.; Brand, S.; Abram, R. A.: Intervalence band absorption in semiconductor laser materials. *Semiconductor Science and Technology*, vol. 1, 2, 1986: p. 116, doi:10.1088/0268-1242/1/2/004.

[39] Knötig, H.; Nauschütz, J.; Opačak, N.; et al.: Mitigating Valence Intersubband Absorption in Interband Cascade Lasers. *Laser & Photonics Reviews*, vol. 16, 9, 2022: p. 2200156, doi:10.1002/lpor.202200156.

[40] Chapter 2 - Theoretical Background. In *Fourier Transform Infrared Spectrometry*, John Wiley Sons, Ltd, 2007, ISBN 9780470106310, p. 19–55, doi:10.1002/9780470106310.ch2.

[41] Jaggi, N.; Vij, D.: FOURIER TRANSFORM INFRARED SPECTROSCOPY. In *Handbook of Applied Solid State Spectroscopy*, Springer US, 2006, ISBN 978-0-387-37590-8, p. 411–450, doi:10.1007/0-387-37590-2_9.

[42] Hilfiker, J.; Woollam, J.: INSTRUMENTATION | Ellipsometry. In *Encyclopedia of Modern Optics*, Elsevier, 2005, ISBN 978-0-12-369395-2, p. 297–307, doi:10.1016/B0-12-369395-0/00833-2.

[43] Jin, L.; Mogi, S.; Muranaka, T.; et al.: Characterization of thin films from reflection and transmission ellipsometric parameters. *Japanese Journal of Applied Physics*, vol. 61, 1, 12 2021, doi:10.35848/1347-4065/ac42af.

[44] Garg, A.; Sharma, R.; Dhingra, V.: Polarization studies in a computer based laboratory. *Latin-American Journal of Physics Education*, vol. 5, 2011: p. 17. URL <https://api.semanticscholar.org/CorpusID:199494406>

[45] Tompkins, H.; Baker, J.; Smith, S.; et al.: Spectroscopic ellipsometry and reflectometry: a user's perspective. 2000, ISBN 0-7803-6252-7, p. II27–II28, doi:10.1109/LEOSST.2000.869717.

[46] Azzam, R. M.; Bashara, N. M.: *Ellipsometry and polarized light*. North-Holland Publishing, 1977, ISBN 978-0444870162.

[47] Negara, C.: Fast Polarization State Detection by Division-of-Amplitude in a Simple Configuration Setup. 2016.

[48] Pimbley, J. M.: Depletion approximation analysis of an exponentially graded semiconductor p-n junction. *IEEE Transactions on Electron Devices*, vol. 35, 11, 1988: p. 1957–1962, doi:10.1109/16.7410.

[49] Feuchter, T.; Thirstrup, C.: High Precision Planar Waveguide Propagation Loss Measurement Technique Using a Fabry-Perot Cavity. *Photonics*, vol. 7(3), 75, 2020, doi:10.3390/photonics7030075.

[50] Roux, S.; Barritault, P.; Lartigue, O.; et al.: Mid-infrared characterization of refractive indices and propagation losses in GaSb/Al_xGa_{1-x}AsSb waveguides. *Applied Physics Letters*, vol. 107, 2015, doi:10.1063/1.4934702.

[51] Revin, D. G.; Wilson, L. R.; Carder, D. A.; et al.: Measurements of optical losses in mid-infrared semiconductor lasers using Fabry-Perot transmission oscillations. *Journal of Applied Physics*, vol. 95, 2004, doi:10.1063/1.1738523.

[52] Mackay, T. G.; Lakhtakia, A.: *The Transfer-Matrix Method in Electromagnetics and Optics*. Synthesis Lectures on Electromagnetics, 1. ed., 2022, ISBN 978-3-031-00894-8, doi:10.1007/978-3-031-02022-3.